Design and applications of single-photon devices based on waveguides coupled to quantum emitters

by

Golam Raqeeb Bappi

A thesis
presented to the University of Waterloo
in fulfillment of the
thesis requirement for the degree of
Master of Applied Science
in
Electrical and Computer Engineering (Quantum Information)

Waterloo, Ontario, Canada, 2016

I hereby declare that I am the sole author of this thesis. This is a true copy of the thesis, including any required final revisions, as accepted by my examiners.

I understand that my thesis may be made electronically available to the public.

Abstract

Engineering photon-photon interactions is fundamentally challenging because photons in vacuum do not interact with each other. While their interactions can be mediated using optical nonlinearities, these effects are negligible for individual photons. This thesis explores two topics related to optical nonlinearities in waveguides. In the first part, we perform a numerical simulation study of hollow core antiresonant reflecting optical waveguides (ARROWs) fabricated using standard lithographic techniques in the context of their suitability as a platform for on-chip photonic quantum information processing. We investigate the effects of the core size, the number of pairs of antiresonant layers surrounding the hollow core, and the refractive index contrast between cladding materials on propagation losses in the waveguide. Additionally, we explore the feasibility of integrating these waveguides with Bragg gratings and dielectric metasurface mirrors to form on-chip cavities, that when loaded with atomic ensembles could act as nonlinear optical devices controllable with single photons.

The second part of this thesis studies the application of a 3 level quantum emitter coupled to a directional optical waveguide to deterministically subtract a single photon from a propagating optical pulse. Subtracting a single photon from a light state is one of the most fundamental operations with important applications in quantum information processing. However, current methods to subtract a photon such as using a low reflectivity beam splitter suffer from inherently low success probabilities as well as a strong dependence on the number of photons in the input. We explore implementing this single photon subtraction operation in our proposed system when the optical input is a continuous wave coherent state, coherent pulsed state containing a finite number of photons, or a Fock state.

Acknowledgements

First I would like to thank my advisor Michal Bajcsy for his support and guidance throughout the course of my research. I am primarily thankful for his undeserved patience, without which the work covered in this dissertation would not have been possible. I would also like to thank my colleagues Jeremy Flannery and Rubayet Al Maruf for the stimulating discussions on the topics I investigated, and Christopher Haapamaki for his nanofabrication advice. I thank the QNC Nanofab team, particularly Nathan Nelson-Fitzpatrick for the indispensable advice throughout my fabrication work on ARROW waveguides. Lastly I would like to thank Professors Na Young Kim and Christopher Wilson for providing feedback on this thesis.

Dedication

This is dedicated to my parents for their love and support.

Table of Contents

List of Tables viii

List of Figures ix

1 Introduction 1

2 ARROW Waveguides 3

2.1 Motivation . . . 3

2.1.1 Total Internal Reflection . . . 3

2.1.2 Hollow core optical fibres . . . 4

2.2 ARROW Principles and Analysis . . . 5

2.3 Fabrication methods . . . 14

2.4 Fabrication challenges . . . 17

2.4.1 Future work . . . 19

3 Field enhancement in hollow core ARROW waveguides 21

3.1 Bragg Gratings . . . 21

3.1.1 Mirrors . . . 24

3.1.2 Cavities . . . 26

3.2 Metasurface cavities . . . 28

4 Single photon extraction **31**

4.1 Motivation . . . 31

4.2 Initial calculations . . . 33

4.3 Coherent pulse calculations . . . 38

4.4 Fock state calculations . . . 42

4.5 Imperfectly directional waveguides . . . 46

5 Conclusion **50**

5.1 ARROW waveguides . . . 50

5.2 Single photon extraction . . . 50

References **52**

APPENDICES **56**

A Mode solver and waveguide parameters **57**

B Python code for single photon extraction **63**

B.1 Continuously driven coherent input . . . 63

B.2 Coherent input pulse . . . 65

B.3 Fock state input . . . 67

List of Tables

A.1 Finite element modelling simulation parameters 57

A.2 Self aligned pedestal ARROW parameters 57

A.3 Layer thicknesses of optimized 3 period hollow core ARROWs using $Si_3N_4(1.74)/SiO_2$ cladding layers for various core sizes 58

A.4 Layer thicknesses of optimized 2 period hollow core ($5.8\mu m \times 12\mu m$) ARROWs with high index layer beneath the core 59

A.5 Layer thicknesses of optimized 3 period hollow core ($5.8\mu m \times 12\mu m$) ARROWs with high index layer beneath the core 59

A.6 Layer thicknesses of optimized 4 period hollow core ($5.8\mu m \times 12\mu m$) ARROWs with high index layer beneath the core 60

A.7 Layer thicknesses of optimized 2 period hollow core ($5.8\mu m \times 12\mu m$) ARROWs with low index layer beneath the core 61

A.8 Layer thicknesses of optimized 3 period hollow core ($5.8\mu m \times 12\mu m$) ARROWs with low index layer beneath the core 61

A.9 Layer thicknesses of optimized 4 period hollow core ($5.8\mu m \times 12\mu m$) ARROWs with low index layer beneath the core 62

List of Figures

2.1 Incident, reflected, and transmitted rays at a waveguide interface. 3

2.2 (a) Bragg fibre, (b) Photonic crystal fibre (Source: [1]), and (c) Kagome fibre (Source: [2]) 5

2.3 Resonance in the core and antiresonance in the cladding confines light within the core. 6

2.4 First generation ARROW shown in (a), prealigned pedestal variant in (b), and self aligned pedestal variant in (c). Figure reproduced from [3]. 9

2.5 (a) Cross section of hollow core ARROW using 3 periods of antiresonant cladding materials ($n_1 = 1.74, n_2 = 1.44$). (b) Fundamental mode profile, and (c) propagation loss spectrum of an optimized hollow core ARROW with a $5.8\mu m \times 12\mu m$ core surrounded by 3 periods of $Si_3N_4(1.74)/SiO_2$ cladding layers. The waveguide is designed for a wavelength of 852 nm. The fringes above ($y > 2.9\mu m$), below ($y < -2.9\mu m$), and beside ($x > 6\mu m$) the core represent the fundamental mode's leakage of power from the core into the cladding layers and out of the waveguide. 10

2.6 Plot of loss versus mode field area for a 3 period hollow core ARROW using $Si_3N_4(1.74)/SiO_2$ cladding layers for various core sizes. 11

2.7 Comparison of the propagation loss for hollow core ARROWs with a $5.8\mu m \times 12\mu m$ core using various cladding material pairs. The design wavelength is 852 nm. 12

2.8 A) ARROW with high index layer beneath the core, B) low index layer beneath the core where $n_1 > n_2$. 13

2.9 Comparison of the propagation loss for the two variants of hollow core ARROWs with a $5.8\mu m \times 12\mu m$ core using different cladding material pairs. The design wavelength is 852 nm. 14

2.10 Hollow core ARROW fabrication using wafer bonding (Source: [4]). 16

2.11 Fabrication process for I. First generation ARROW, II. Prealigned pedestal ARROW, and III. Self aligned pedestal ARROW. Figure reproduced from [3]. 16

2.12 The cross sections of SU8 cores with (a) silicon nitride and (b) silicon oxide films deposited on top were imaged using the Raith 150 electron beam lithography tool. The silicon nitride samples have a conformality ratio of ~ 1.3. The silicon oxide samples on the left and right have conformality ratios of 1.69 and 1.28 respectively. 18

2.13 Procedure to create the pedestal using a protective metal layer on top of the SU8 core. (Source: [3]) 18

2.14 Chromium on SU8 core obtained using the procedure depicted in Figure 2.13. 19

3.1 Etched gratings in the various antiresonant layers: (A) first layer above the core, (B) first layer beneath the core, (C) top layer. (D) Schematic of ARROW Bragg grating implemented using the first antiresonant layer beneath the core. 22

3.2 Change in the effective index of propagation for a hollow core ARROW with a $5.8\mu m \times 12\mu m$ core using 3 periods of $Si_3N_4(1.74)/SiO_2$ antiresonant layers. The x-axis refers to the etch depth relative to the original thickness of that particular layer. 23

3.3 Normal incidence of a plane wave on a multilayer dielectric stack. Given the transmitted field, the incident and reflected fields can be calculated using MSE. 24

3.4 (a) Mirror reflectivites of the possible ARROW Bragg gratings. Dotted lines denote the maximum reflectivity for a particular grating. The relative etch depths for the layer above the core, layer beneath the core, and top layer are 74%, 70%, and 68% respectively. (b) Using MSE with plane wave incidence, we obtain the reflectivity spectrum of a 10000 period Bragg mirror created by periodically etching the antiresonant layer beneath the core. The etch depth is 70% of this layer, which creates an effective propagation index contrast of 5×10^{-4} with a 8% increase in loss. 25

3.5 (a) Field intensity enhancement in a cavity using a half wavelength spacer for various grating mirror periods. (b) Electric field intensity distribution throughout the cavity with 7000 period Bragg mirrors. z = 0 marks the start of the cavity with the field being 1. (c) Schematic of proposed ARROW waveguide cavity with integrated Bragg grating mirrors. 27

3.6 A photonic crystal membrane may act as a mirror for light that is incident perpendicular to the plane. 28

3.7 Cooperativity of hollow core ARROW ($A_{mode} = 18\mu m^2$) cavity formed using dielectric metasurface mirrors for various waveguide lengths and mirror reflectivities. 30

4.1 Schematic of single photon extraction using single-photon Raman interaction (SPRINT) [5]. Γ is the spontaneous emission rate into a resonator mode. 31

4.2 Overview of a 3 level system coupled to a chiral waveguide. 32

4.3 Output values of the various operators given a continuous wave coherent input. 38

4.4 Output values for a coherent pulsed input state. 40

4.5 The probability of extracting a single photon is a function of the τV^2 product. 41

4.6 The probability of single photon extraction as a function of the interaction product and the number of photons in the input. 41

4.7 Output values for a $N = 10$ Fock state input. 43

4.8 Probability of extracting a single photon from a Fock state. 44

4.9 Comparison of the probability of single photon extraction from a coherent pulsed state (triangles) and a Fock state (squares). 45

4.10 Comparison of the probability of single photon extraction from a coherent pulsed state (triangles) and a Fock state (squares) with a non-zero decay rate of the emitter. 45

4.11 Overview of a 3 level system coupled to a non perfect chiral waveguide. . . 46

4.12 Comparison of the probability of single photon extraction via the left channel from a coherent pulsed state (triangles) and a Fock state (squares) with $\beta = 0.75$. 48

4.13 Comparison of the probability of single photon extraction via the left channel from a coherent pulsed state (triangles) and a Fock state (squares) using a nondirectional waveguide. 49

Chapter 1

Introduction

Realizing interactions between single photons has long been a difficult goal of optical science, given that photons in vacuum do not interact with each other. However, effective photon-photon interactions can be implemented through the use of optical nonlinearities. While optical nonlinearities can be found in a range of systems, they can be close to negligible at electric fields associated with individual photons. Optical waveguides offer an excellent platform for enhancing optical nonlinearities by increasing the field of a single photon through transverse confinement. Additionally, the optical nonlinearities can be further enhanced by confining the photons longitudinally, by increasing the light-matter interaction time, and through the use of coherent control techniques. This work explores two topics related to optical nonlinearities in optical waveguides.

The first topic investigates the design of antiresonant reflection on-chip hollow core waveguides and the feasibility of adding new functionalities to such waveguides. Filled with ensembles of quantum emitters such as dilute gas at room temperature or laser cooled atoms, on-chip hollow core waveguides have the potential to become building blocks for scalable optical devices operating with single photons given their relatively low propagation losses and small optical mode areas (Figure 2.6). Several notable demonstrations of strong light-matter interaction in hollow core waveguides have been reported in recent years, such as all optical switching with a few hundred photons in a hollow core photonic crystal fibre with laser cooled atoms [6], cross-phase modulation with few photons [7], and single photon broadband quantum memory [8] in a photonic crystal fibre filled with room temperature alkali atoms, as well as demonstration of quantum state control of warm alkali vapor in a hollow core antiresonant section optical waveguide on a chip [9].

In Chapter 2 we introduce the principles of operation of antiresonant reflecting optical

waveguides (ARROW). We study how the propagation losses of hollow core ARROW waveguides are affected for various core sizes, cladding material pairs, and number of periods of antiresonant layers. We also give an overview of their fabrication, along with our results. In Chapter 3, we study how grating structures can be implemented within these hollow core waveguides to possibly create mirrors and cavities to enhance the electric field. We will also look at integrated cavities created using highly reflective photonic crystal membrane mirrors attached to hollow core ARROW waveguides, and determine the strength of light-matter interaction.

The second topic studies the behaviour of a single 3 level quantum emitter coupled to a directional optical waveguide and the application of this system for subtracting single photons from light propagating in the waveguide. Deterministic single photon operations have long been a goal of fundamental science and quantum information processing [10]. Subtracting a single photon from a state of light could be intuitively seen as one of the most basic of such operations but it is actually surprisingly complicated both in its operator description and its experimental implementation. While it can be typically done with a low reflectivity beam splitter, the success probability of extracting exactly one photon is inherently low and depends on the number of photons present [11]. Deterministic single photon subtraction was recently demonstrated by Rosenblum et al. [5] with a Λ scheme atom coupled to the evanescent field of a nanofibre coupled microsphere resonator. However recent demonstrations of a novel type of chiral waveguide [12] presents another way to implement these single photon operations. In these waveguides the polarization of the photon determines the direction of propagation. Coupling these waveguides to a 3 level atom is a promising approach to investigate the implementation of single photon operations.

In Chapter 4 we study the dynamics of a chiral waveguide coupled to a 3 level quantum emitter for deterministic single photon extraction from an optical pulse. We begin by looking at the case of a continuously driven coherent input, which can be solved analytically. Next we study the pulsed coherent and Fock state input cases using numerical analysis.

Chapter 2

ARROW Waveguides

2.1 Motivation

2.1.1 Total Internal Reflection

Optical waveguides have traditionally been based on the principle of total internal reflection (TIR). Here, light is confined to a high refractive index core surrounded by lower index cladding layers as shown below where $n_1 > n_2$.

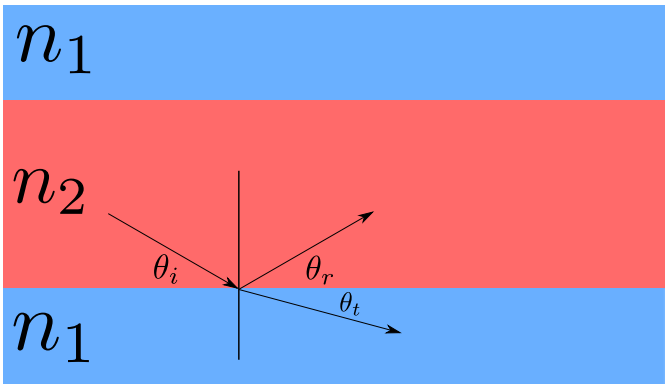

Figure 2.1: Incident, reflected, and transmitted rays at a waveguide interface.

The relation between the incident and transmitted angle is given by Snell's Law.

$$n_1 \cos(\theta_i) = n_2 \cos(\theta_t) \tag{2.1}$$

Given that the minimum angle of the refracted light is 0°, the critical incident angle is given by

$$\theta_{critical} = \arccos\left(\frac{n_2}{n_1}\right) \tag{2.2}$$

Below this critical incident angle, light does not propagate in the cladding material and is totally internally reflected. Solid core optical fibres are one example of a device where waveguiding is based upon TIR. The main drawback of TIR is that it cannot be used to guide light when the refractive index of the core is less than that of the cladding. In that case for all incident angles, light will refract into the cladding and the power in the core will quickly leak out. Given that there does not exist a material with refractive index lower than that of air ($n = 1$), hollow core waveguides cannot operate based on TIR.

2.1.2 Hollow core optical fibres

Optical confinement in a waveguide can also based upon interference effects along the transverse direction. The Bragg fibre utilizing a 1D photonic crystal was first proposed by Yeh *et al.* [13] in 1978. The multiple partially transmitted and reflected waves in the cladding interfere destructively which leads to high reflection of light into the core. Figure 2.2a shows the cladding which is composed of concentric periodic alternating dielectric layers which act as a highly reflective mirror for a wide range of incident angles, leading to a low loss waveguide. However these fibres have large cross sections, and thus large mode areas. For enhanced light-matter interaction with loaded atomic gases, both low losses and small optical mode areas are required.

Interference effects can also be used to confine light when the cladding region consists of a 2D periodic lattice of holes in silica as shown in Figure 2.2b. The size of the holes, their shape, and the spacing between them determines the optical properties of this "photonic crystal" region. Light cannot propagate along the transverse direction due to the photonic band gap in frequencies where there is no real wavevector solution. Thus, it evanescently decays into the cladding, but still propagates along the core. Fundamental mode losses as low as 1.2 dB/km [14] have been reported which is almost as low as the 0.15 dB/km [15] that has been achieved in conventional fibres. These hollow core photonic crystal fibres

(HC-PCFs) have small mode areas and low losses which make them ideal for engineering single atom-photon interactions.

Another class of hollow core photonic crystal fibres are Kagome fibres which operate on the principle of inhibited coupling (IC) guidance [2]. Figure 2.2c shows the fibre which is designed such that there are modes guided within the hollow core as well as a continuum of modes supported by the cladding. The significant phase mismatch between the core and cladding modes prevents light in the core from leaking into the cladding [16].

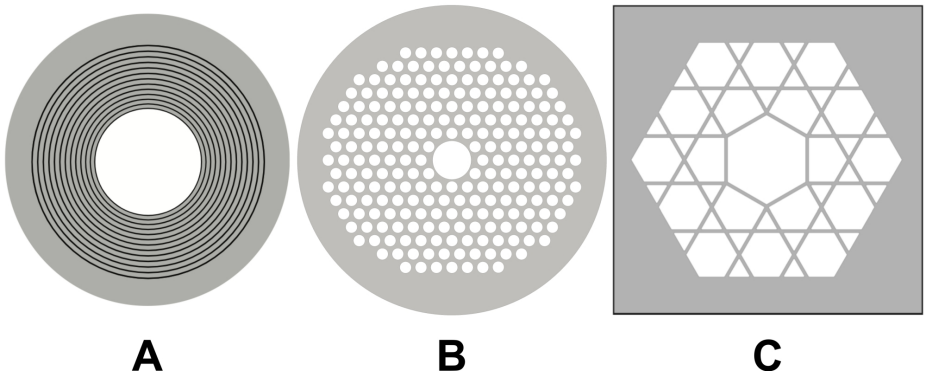

Figure 2.2: (a) Bragg fibre, (b) Photonic crystal fibre (Source: [1]), and (c) Kagome fibre (Source: [2])

The light-matter interaction could be further enhanced by additional control over the photonic environment, which is not easily possible with these fibre based geometries. Moving to a planar on-chip platform will allow us to introduce structures for dispersion engineering, integrated mirrors and cavities, and atom trapping and cooling infrastructure. This will open up new ways for us to study fundamental quantum optics phenomena and their practical applications.

2.2 ARROW Principles and Analysis

Antiresonant reflection optical waveguides (ARROWs) were first proposed and demonstrated by Duguay *et al.* [17] in 1986 for light propagation in low index media. ARROWs consist of a core surrounded by multiple dielectric layers whose thicknesses are chosen such that there is destructive interference of the multiple incident and reflected waves in each cladding layer, and constructive interference in the core for a given wavelength. The

cladding acts as a highly reflective mirror that confines light to the core and results in low loss propagation. The initial demonstration guided light in a silicon dioxide core using a single pair of Si/SiO_2 antiresonant layers below and total internal reflection from the air above for confinement. Hollow core ARROW waveguides were first demonstrated by Delonge and Fouckhardt [18] in 1995. Since then ARROWs have found applications in lasers [19], single molecule detection [20], and have been used to demonstrate electromagnetically induced transparency and slow light on a chip [9]. Here we will explain the principles behind the ARROW [17] shown in Figure 2.3.

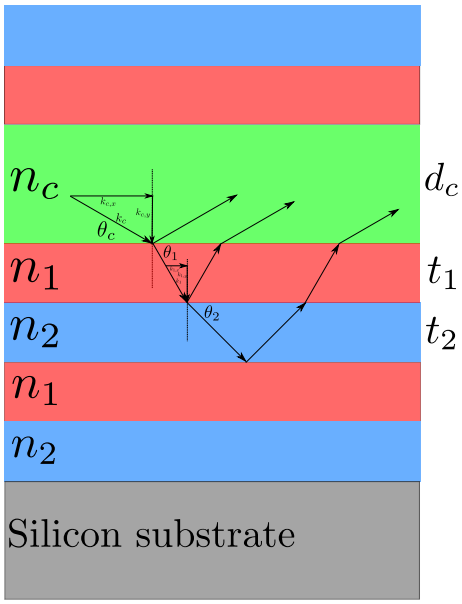

Figure 2.3: Resonance in the core and antiresonance in the cladding confines light within the core.

In order to maximize the field intensity within the core, there must be constructive interference of the incident and reflected waves.

$$2k_{c,y}d_c + 2\phi_1 = 2m\pi$$
$$2n_c k_0 \sin(\theta_c)d_c + 2\phi_1 = 2m\pi$$

where ϕ_1 is the phase shift of the reflected wave at the interface between the core and the first cladding layer. If the core is hollow ($n_{core} = 1$), then the reflected wave obtains a π phase shift and we have that

$$
\begin{aligned}
2n_c k_0 \sin(\theta_c) d_c &= 2(m-1)\pi \\
\frac{2\pi n_c}{\lambda} \sin(\theta_c) d_c &= (m-1)\pi \\
\sin(\theta_c) &= \frac{(m-1)\lambda}{2n_c d_c}
\end{aligned}
$$

Finally for the fundamental mode, we have

$$
\sin(\theta_c) = \frac{\lambda}{2n_c d_c} \tag{2.3}
$$

In the cladding layers, we must have destructive interference so that light leakage from the core is minimized. In the j^{th} layer, we must have that

$$
2n_j k_0 \sin(\theta_j) t_j + 2\phi_j = 2\left(m + \frac{1}{2}\right)\pi \tag{2.4}
$$

If layer i is surrounded by lower refractive index layers, then the phase shift of the reflected wave from those interfaces is 0. Otherwise if the refractive index of the surrounding layers is greater, then the phase shift of the reflected wave from those interfaces is π. The general condition can then simply be written as

$$
\begin{aligned}
2n_i k_0 \sin(\theta_i) t_i &= 2\left(N + \frac{1}{2}\right)\pi \\
\frac{2\pi n_i}{\lambda} \sin(\theta_i) t_i &= \left(N + \frac{1}{2}\right)\pi
\end{aligned}
$$

Using Snell's Law, we know that

$$
\begin{aligned}
n_i \cos(\theta_i) &= n_c \cos(\theta_c) \\
\cos(\theta_i) &= \frac{n_c}{n_i} \cos(\theta_c)
\end{aligned}
$$

and using the identity $\cos^2(\theta) + \sin^2(\theta) = 1$,

$$\begin{aligned}
\sin(\theta_i) &= \sqrt{1 - \frac{n_c^2}{n_i^2}\cos^2(\theta_c)} \\
&= \sqrt{1 - \frac{n_c^2}{n_i^2}\left(1 - \frac{\lambda^2}{4n_c^2 d_c^2}\right)} \\
&= \sqrt{1 - \frac{n_c^2}{n_i^2} + \frac{\lambda^2}{4n_i^2 d_c^2}}
\end{aligned}$$

Combining this with the previous equation, we obtain the thickness of each layer for the antiresonance condition to be satisfied.

$$t_i = \frac{\lambda}{4n_i}(2N+1)\left(1 - \frac{n_c^2}{n_i^2} + \frac{\lambda^2}{4n_i^2 d_c^2}\right)^{-\frac{1}{2}} \tag{2.5}$$

We note that the antiresonance condition differs slightly from the Bragg condition for normal incidence ($t_i = \lambda/4n_i$).

One of the advantages of ARROWs is that the cladding layers do not need to be periodic with respect to the refractive index or their thicknesses as long as they satisfy the antiresonance condition specified in Equation 2.5. Although for the sake of simplicity, here we will only consider two different materials to be used for the cladding layer. As shown by Duguay [17], while a single pair of cladding layers was sufficient to achieve low loss propagation in the core, adding more layers should reduce the loss further.

The loss of the waveguide can be estimated using the transfer matrix method [21]. This method takes the 1D refractive index profile of the waveguide and calculates the propagation loss. This is done by calculating the reflectivity of the dielectric stacks surrounding the core given the incident glancing angle (Equation 2.3). The propagation losses of the TE-like and TM-like waves with respect to the vertical and horizontal directions respectively are estimated as

$$\alpha_{vertical} = \frac{2 - R_{top} - R_{bottom}}{2h_c}\tan(\theta_{c,vertical}) \tag{2.6}$$

$$\alpha_{horizontal} = \frac{2 - R_{left} - R_{right}}{2w_c}\tan(\theta_{c,horizontal}) \tag{2.7}$$

where h_c is the height of the core, w_c is the width of the core, $\theta_{c,vertical}$ is the glancing angle along the vertical direction, and $\theta_{c,horizontal}$ is the glancing angle along the horizontal direction. Given that the ARROW has a 2D refractive index profile, its propagation loss (Equation 2.8) can be estimated as the average of the losses of the two 1D cross sectional profiles. This technique allows us to design waveguides that are polarization sensitive given that TE and TM waves have different reflection coefficients.

$$\alpha_{waveguide} = \frac{\alpha_{vertical} + \alpha_{horizontal}}{2} \tag{2.8}$$

The dielectrics used for the cladding layers have included $Si_3N_4 (n = 1.7 - 2)$, SiO_2 $(n = 1.44)$, TiO_2 $(n = 2.1)$, and Ta_2O_5 $(n = 2.4)$. A Si_3N_4/SiO_2 pair has been commonly used [3, 22, 23], although a combination of TiO_2 [18] or Ta_2O_5 [24] along with SiO_2 has been explored as well. Si_3N_4 has been typically used as as the high index antiresonant layer given that its ease of deposition using plasma enhanced chemical vapor deposition (PECVD), relatively high refractive index ($n = 1.7 - 2$, depending on the deposition parameters), and negligible absorption in the desired optical range [25].

There are 3 different types of ARROWs that have been developed. They are the regular ARROW, prealigned pedestal (PAP) ARROW, and self aligned pedestal (SAP) ARROW as shown in Figure 2.4. The self aligned pedestal ARROWs which have air as the terminating layer on both sides have been found to have the lowest losses [23]. Numerically, the losses for the three variants using Si_3N_4/SiO_2 for the antiresonant layers and a $5.8\mu m \times 12\mu m$ core, were found to be $7.23cm^{-1}$, $1.09cm^{-1}$, and $0.36cm^{-1}$ respectively while experimentally the losses for these variants were found to be $9.5cm^{-1}$, $4.2cm^{-1}$, and $2.2cm^{-1}$ respectively [3]. The higher experimental losses arise due to deviation of the cladding layer thicknesses from the ideal values, and the surface roughness which increases the scattering losses. Given the lower losses, only the SAP variant hollow core ARROW will be considered in our analysis.

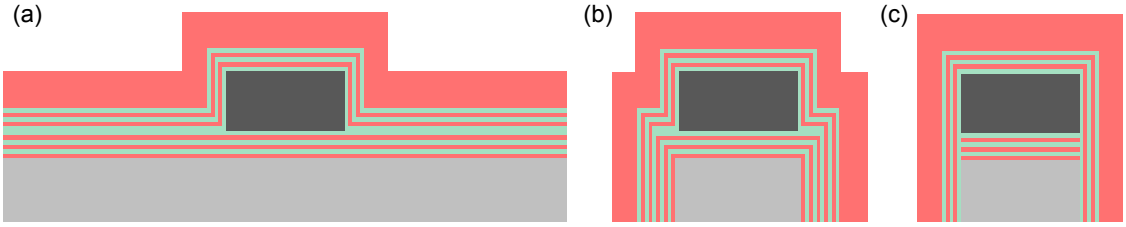

Figure 2.4: First generation ARROW shown in (a), prealigned pedestal variant in (b), and self aligned pedestal variant in (c). Figure reproduced from [3].

In addition to the transfer matrix method, the modal characteristics of the ARROW can also be found using photonic modelling software such as the finite element solver FemSIM by RSoft. The main source of loss in these waveguides is due to the fundamental leaky mode. This can be minimized by using higher refractive index contrast cladding materials or a larger number of antiresonant layers, and optimizing the thickness of each cladding layer using the RSoft MOST optimization tool. The waveguide loss can be calculated from the imaginary part of the effective propagation index of the fundamental mode using

$$\alpha = \frac{4\pi Im\{n_{eff}\}}{\lambda} \tag{2.9}$$

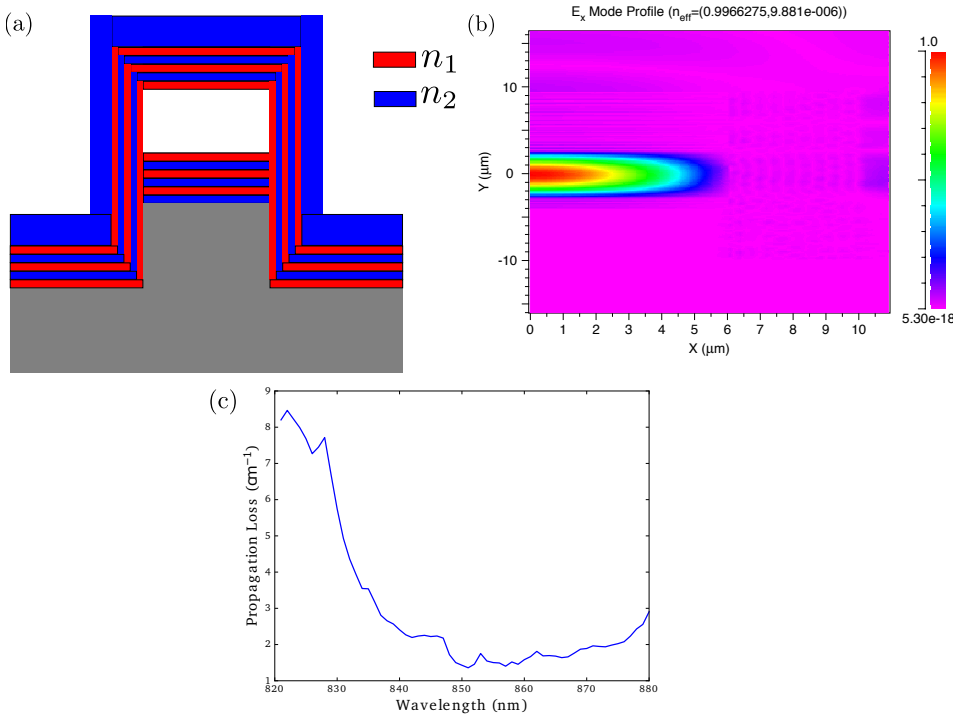

Figure 2.5: (a) Cross section of hollow core ARROW using 3 periods of antiresonant cladding materials ($n_1 = 1.74, n_2 = 1.44$). (b) Fundamental mode profile, and (c) propagation loss spectrum of an optimized hollow core ARROW with a $5.8\mu m \times 12\mu m$ core surrounded by 3 periods of $Si_3N_4(1.74)/SiO_2$ cladding layers. The waveguide is designed for a wavelength of 852 nm. The fringes above ($y > 2.9\mu m$), below ($y < -2.9\mu m$), and beside ($x > 6\mu m$) the core represent the fundamental mode's leakage of power from the core into the cladding layers and out of the waveguide.

The core dimensions also affect the propagation loss. We can reduce the optical mode area by reducing the core width. However the light will then propagate at a larger glancing angle relative to the sidewalls according to Equation 2.3. For the fundamental TE mode, the light has TM-like polarization relative to the sidewalls. Due to the same phenomenon that gives rise to the Brewster angle, the reflectivity of the TM-like waves off the sidewalls will be lower, thus increasing the propagation loss. This is why the width of the core is typically chosen to be larger than its height. In Figure 2.6 we show how the propagation loss increases as we decrease the core size. The optical mode area is defined as

$$A_{mode} = \frac{\iint \epsilon(x,y)|E(x,y)|^2 dxdy}{\max\{\epsilon(x,y)|E(x,y)|^2\}} \tag{2.10}$$

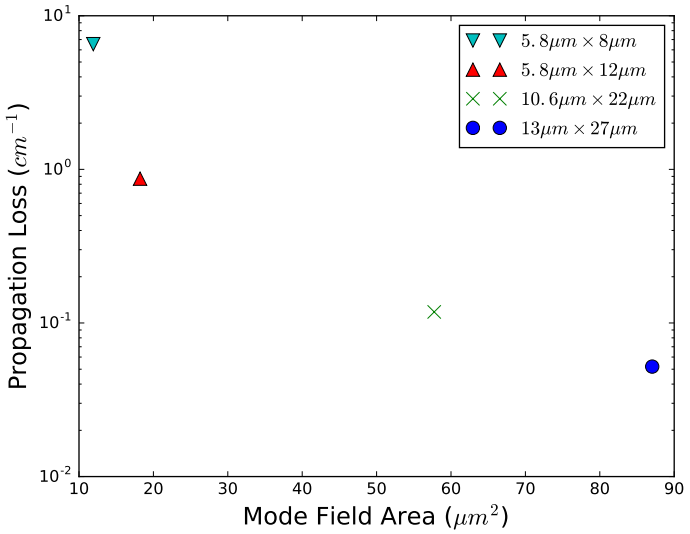

Figure 2.6: Plot of loss versus mode field area for a 3 period hollow core ARROW using $Si_3N_4(1.74)/SiO_2$ cladding layers for various core sizes.

All the ARROW waveguides studied thus far place the high index layer adjacent to the core because of the larger Fresnel reflection coefficient given by

$$R = \left| \frac{n_c \sin(\theta_c) - n_1 \sin(\theta_1)}{n_c \sin(\theta_c) + n_1 \sin(\theta_1)} \right|^2 \tag{2.11}$$

where a larger refractive index difference between core and adjacent layer leads to a higher reflectivity. Due to the symmetry of the waveguide about the vertical axis, the mode profile (Figure 2.5a) is symmetric as well. The simulation parameters for the finite element solver are given in Appendix A where the design wavelength is chosen to be 852 nm. We also obtain the propagation loss spectrum in Figure 2.5b and observe that the loss is minimized at the design wavelength.

In Figure 2.7, using finite element modeling and the optimization tool by RSoft, we determine the minimum achievable propagation loss for hollow core ARROW waveguides for different antiresonant material pairs, and using 2, 3, 4 periods of these layers surrounding the core. These loss values were found by first choosing the thicknesses of the cladding layers according to the antiresonance condition given by Equation 2.5, and locating the fundamental quasi-Gaussian mode of the waveguide. Using this mode as a seed, an optimization procedure is performed whereby the thicknesses of each layer are varied according to a genetic algorithm. Slowly the loss is minimized and the optimization tool determines the corresponding cladding layer thicknesses to achieve it.

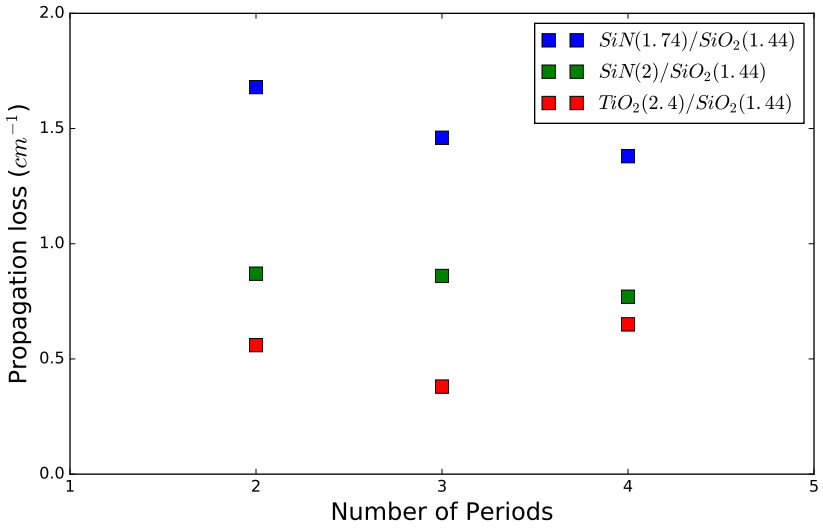

Figure 2.7: Comparison of the propagation loss for hollow core ARROWs with a $5.8\mu m \times 12\mu m$ core using various cladding material pairs. The design wavelength is 852 nm.

We find that the propagation loss of the ARROW can be lowered by using higher refractive index contrast cladding material pairs, or by increasing the number of periods of

antiresonant layers surrounding the core. We observe that adding more periods does not necessarily yield a steady decrease in the mode loss (ie. going from 2 to 3 periods decreases the loss more than by going from 3 to 4 periods). There seems to be a lower bound on the loss for a given material pair as well. It should be noted that the 4 period TiO_2/SiO_2 waveguide loss could not be lowered below that of the 3 period version during the multiple optimization runs. However, we believe that with some more tweaking of the optimization parameter space, this should be possible.

The waveguides in Figure 2.7 and in the literature [3, 18, 22, 23, 24, 25, 4] surround the core with the high index layer as shown in Figure 2.8a because it is intuitively expected for the higher Fresnel reflection coefficient at the interface to result in a lower overall waveguide loss. However another possibility that has not yet been explored is to have the layer immediately beneath the core be the low index layer as shown in Figure 2.8b. The propagation losses of the optimized waveguides for this variant is compared with that of the typical configurations in Figure 2.9.

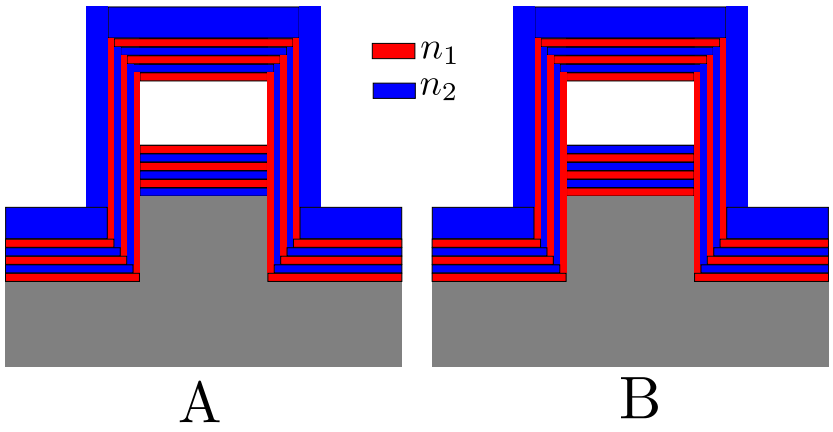

Figure 2.8: A) ARROW with high index layer beneath the core, B) low index layer beneath the core where $n_1 > n_2$.

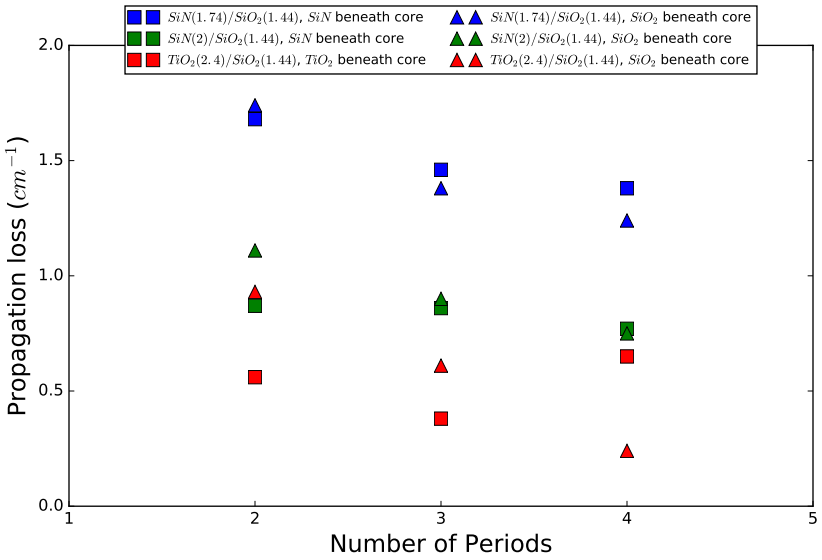

Figure 2.9: Comparison of the propagation loss for the two variants of hollow core ARROWs with a $5.8\mu m \times 12\mu m$ core using different cladding material pairs. The design wavelength is 852 nm.

We find that there is not a significant difference in the propagation loss between the two variants given the same cladding material pair, and number of antiresonant layers used. In each case, the waveguides can be optimized such that they have comparable propagation losses. It should be noted that the loss of the 4 period TiO_2/SiO_2 waveguide using TiO_2 below the core could not be lowered below that of the 3 period version during the multiple optimization runs. However, we believe that with some more tweaking of the optimization parameter space, this should be possible. The cladding layer thicknesses for all the waveguides in Figure 2.9 are given in Appendix A.

2.3 Fabrication methods

There are two main methods to fabricate hollow core ARROWs. The first method reported by Bernini *et al.* [4] uses silicon to silicon wafer bonding as shown in Figure 2.10. Initially a square groove is etched into the silicon wafer, followed by deposition of the bottom antiresonant layers. The top layers are deposited onto another wafer. The two pieces are

then wafer bonded to create the hollow core waveguide. These devices have achieved losses as low as $6.7cm^{-1}$, but the large core size ($130\mu m \times 130\mu m$) is not particularly suitable for applications trying to achieve optical mode areas closer to those found in single-mode optical fibres. The second method, explored extensively by the Schmidt group at UC Santa Cruz and the Hawkins group at BYU, uses a bottom-up fabrication process with a sacrificial core material which is later removed to create the hollow core.

Figure 2.11-I shows the fabrication process for the first generation of hollow core ARROWs. The first step is to deposit the bottom antiresonant layers using PECVD. This is followed by deposition of the sacrificial layer and photolithography to pattern the core. Using aluminum as the core material has been investigated [26], but it tended to have a trapezoidal shape instead of the desired rectangular profile. Multiple positive and negative photoresists [22] have been investigated for the core material, but SU-8 is typically used due to the fact that it can be hard baked to prevent it from reflowing when placed in the high temperature PECVD chamber [25]. After patterning the sacrificial core, the top antiresonant layers are deposited. The top layer is chosen to be significantly thicker than the other ones for mechanical stability. Finally, the sacrificial core material is removed to create the hollow core. One drawback of using PECVD to deposit the top antiresonant layers is the nonconformal deposition process, whereby layers on top of the core are thicker than those on the sides [23]. Characterizing this ratio t_h/t_v allows one to account for it when modelling the waveguide.

There have been some variations of this first generation fabrication process to decrease the loss of the waveguide by having an air terminating layer on the sides [3]. One variant is known as the prealigned pedestal (PAP) ARROW. As shown in Figure 2.11-II, initially a pedestal with the core width is created on the substrate using a photolithography and etch process before depositing the bottom layers. Another variant is the self-aligned pedestal (SAP) ARROW depicted in Figure 2.11-III. After the core is patterned, it is used as a mask to create the pedestal by etching through the bottom antiresonant layers and a portion of the substrate depending on the desired pedestal height. The pedestal height must be greater than the total thickness of the cladding layers above the core so that the core has an air terminating layer on both sides. A pedestal height of $6\mu m$ has been shown be sufficient given the cladding layer thicknesses of optical hollow core ARROWs but larger pedestals are possible as well. During etching, the core can be protected using a thin metal layer such as chromium or nickel on top. This is needed to prevent the core surface on top from being roughened when creating the pedestal in order to minimize scattering losses in the final hollow core waveguide.

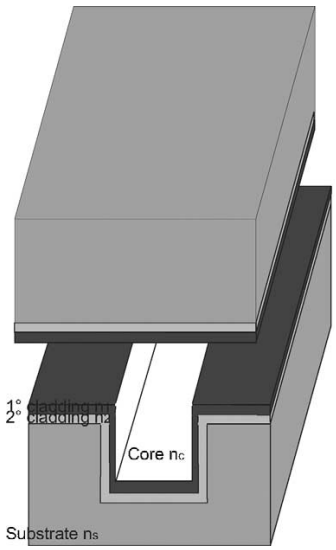

Figure 2.10: Hollow core ARROW fabrication using wafer bonding (Source: [4]).

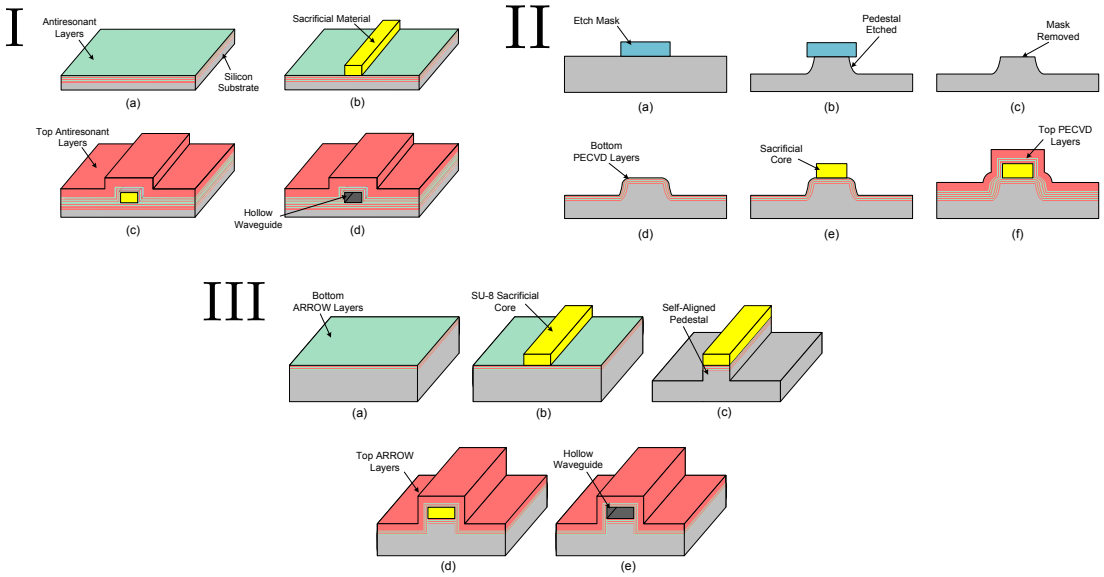

Figure 2.11: Fabrication process for I. First generation ARROW, II. Prealigned pedestal ARROW, and III. Self aligned pedestal ARROW. Figure reproduced from [3].

2.4 Fabrication challenges

We encountered multiple challenges when trying to fabricate self aligned pedestal hollow core ARROW waveguides which have been found to have the lowest losses [25]. We chose to use silicon nitride and silicon oxide ($n = 1.44$) cladding layers given their availability in the Quantum Nanofab PECVD tool. However the refractive index of the silicon nitride film was much lower ($n = 1.74$) than what has been reported ($n = 2 - 2.1$) in the literature [22, 25]. This is not desirable because as we discussed in Section 2.2, using lower refractive index contrast cladding materials increases the loss of the waveguide. We also found that while the conformality ratio of silicon nitride films was fairly consistent, those of silicon oxide films varied widely over multiple cores on the same substrate as shown in Figure 2.12. This made it difficult to model the waveguide because we need to assume a constant confomality ratio for both materials. We believe that a thorough investigation of the deposition parameters (gas flow rates, temperature, pressure, RF power) would have allowed us to minimize the variance in the conformality ratio of silicon oxide films.

To pattern the sacrificial core, we used SU8 which is an epoxy based negative photoresist. This particular photoresist was chosen because it could be hard baked such that it does not reflow [3] at the PECVD deposition temperature ($\sim 250^o$) and deform the desired rectangular shape of the core. However we discovered that the SU8 core had poor adhesion to silicon nitride films, whereby it was washed out during the development step. While the SU8 core had excellent adhesion to the silicon substrate, we believe that the silicon nitride deposition recipe (30 sccm SiH_4 : 900 sccm N_2) contributed to a lower ratio of silicon to nitrogen in the film which resulted in poor adhesion. The lower concentration of silicon atoms most likely resulted in the relatively low refractive index of the film as well. However we also found that the SU8 core adhered well to silicon oxide films. This motivated us to explore how the propagation loss is affected when a silicon oxide layer is used beneath the core rather than silicon nitride. In Figure 2.9 we showed that an optimized waveguide for either case had comparable losses, thus removing the poor adhesion of SU8 to silicon nitride films as a barrier to fabrication.

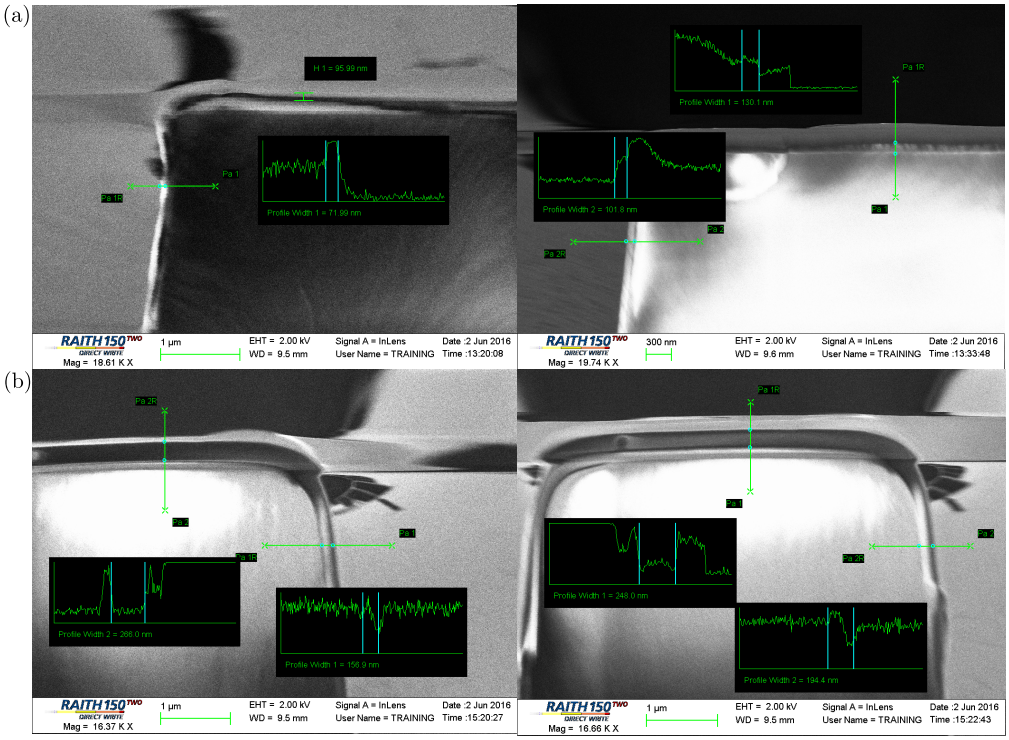

Figure 2.12: The cross sections of SU8 cores with (a) silicon nitride and (b) silicon oxide films deposited on top were imaged using the Raith 150 electron beam lithography tool. The silicon nitride samples have a conformality ratio of ~ 1.3. The silicon oxide samples on the left and right have conformality ratios of 1.69 and 1.28 respectively.

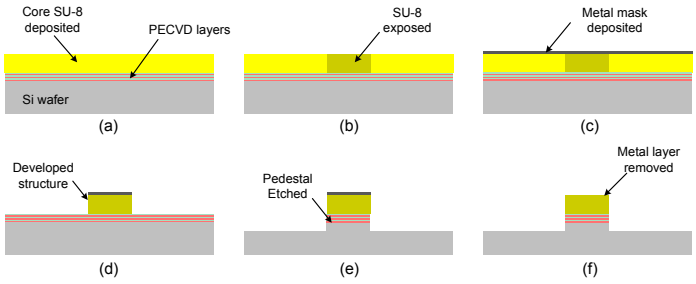

Figure 2.13: Procedure to create the pedestal using a protective metal layer on top of the SU8 core. (Source: [3])

Creating the self aligned pedestal itself as shown in Figure 2.11-III presented yet another challenge. In order to protect the top surface of the core from being roughened during etching, we needed to deposit a thin metal layer on top. As shown in Figure 2.13, the metal can be deposited just before developing the SU8 core. During development the unexposed resist should dissolve, leaving only the core with a metal layer on top of it. Next, deep reactive-ion etching (DRIE) can be used to etch through the bottom antiresonant layers and the substrate underneath to create the pedestal. We chose to use chromium for the protective metal layer because it is highly etch resistant [27], and available for deposition in the Quantum Nanofab using electron beam evaporation. We were able to successfully obtain a chromium layer on top of the SU8 cores as seen in Figure 2.14.

Figure 2.14: Chromium on SU8 core obtained using the procedure depicted in Figure 2.13.

2.4.1 Future work

The next step to successfully fabricate low loss hollow core ARROW waveguides is minimizing the variance in the conformality ratio of silicon oxide films. This requires exploring how the deposition parameters (gas flow rates, pressure, temperature, RF power) affect

the uniformity of the film over a substrate and its conformality. The refractive index of PECVD silicon nitride can be increased by decreasing the flow rate of N_2 to incorporate more silicon atoms into the film. This offers another way to lower the loss of the waveguide as discussed in section 2.2. Once the fabrication process for the waveguides has been optimized, further work remains to try and implement a Bragg grating into them. This is best done using electron beam lithography to create the mask, followed by deep reactive ion etching (DRIE) to etch a grating into a particular antiresonant layer as shown in Figure 3.1.

Chapter 3

Field enhancement in hollow core ARROW waveguides

For a single atom in the hollow core ARROW waveguide, its probability of interaction with a single photon is given by $p = \sigma^2/A \approx \mu E^2 \tau / A$ where μ is the atomic dipole moment, E is the electric field of the photon, τ is the interaction time, and A is the optical mode area. This probability can be very small for wavelengths associated with atomic transitions. We can use to increase the probability of interaction using two methods. We can place the atom in a cavity so that the photon has multiple chances to interact as it travels back and forth. Another option would be to slow down the incoming photon so that it has more time to interact with the atom. This can be done with the use of grating structures. Here we will discuss ways to implement gratings within hollow core ARROW waveguides to possibly create mirrors, cavities, and change the dispersion properties to slow light. We will also analyze a novel type of cavity created using highly reflective dielectric metasurface mirrors attached to these hollow core waveguides.

3.1 Bragg Gratings

For solid core fibres, mirrors and dispersion engineering may be realized using fibre Bragg gratings (FBG) which are implemented by periodically modulating the refractive index in the core [28]. This is not possible with hollow core waveguides because their core is empty, hence there is no material that can be modified. With hollow core ARROWs, we can instead implement a grating by modulating the effective index of propagation. We

propose to do this by etching a grating in the various antiresonant layers. The waveguide will then have a slightly different propagation index along the section where one of cladding layers above or below the core has been etched. Given that the ARROW has a bottom up fabrication process, the grating can be implemented in any particular layer. This has the advantage of leaving the hollow core unobstructed so that atomic ensembles can be loaded inside. As shown in Figure 3.1, we will consider cases where the grating is etched either into the layer immediately above the core, the layer beneath the core, or the very top layer. For the 3 period $Si_3N_4(1.74)/SiO_2$ hollow core ARROW, Figure 3.2 shows how the effective index of propagation changes along the etched region for the 3 different types of gratings.

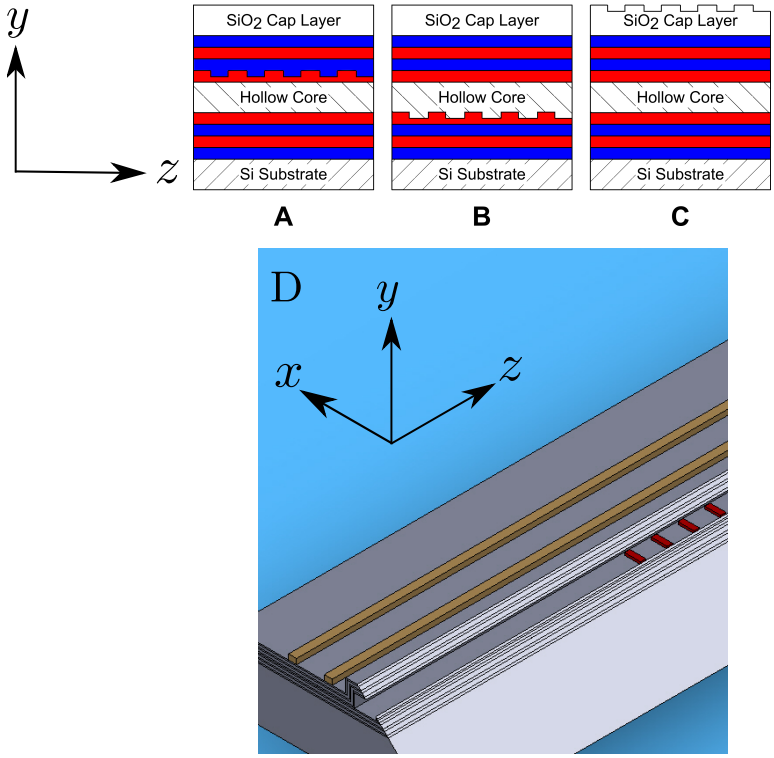

Figure 3.1: Etched gratings in the various antiresonant layers: (A) first layer above the core, (B) first layer beneath the core, (C) top layer. (D) Schematic of ARROW Bragg grating implemented using the first antiresonant layer beneath the core.

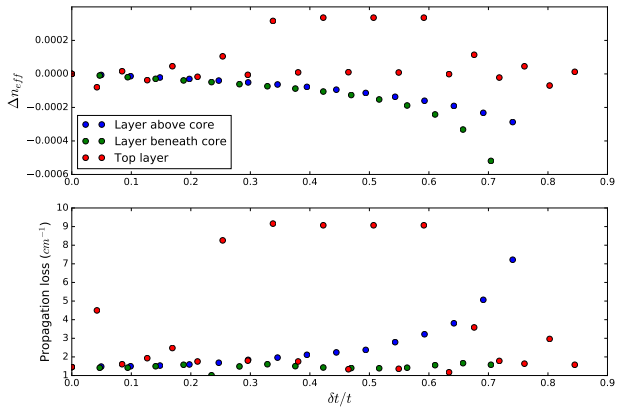

Figure 3.2: Change in the effective index of propagation for a hollow core ARROW with a $5.8\mu m \times 12\mu m$ core using 3 periods of $Si_3N_4(1.74)/SiO_2$ antiresonant layers. The x-axis refers to the etch depth relative to the original thickness of that particular layer.

We see that changing the thickness of a particular antiresonant layer increases the propagation loss because the waveguide is no longer optimized. Layers closer to the core have a greater overlap with the fundamental leaky mode, hence etching them creates a larger perturbation relative to the original waveguide. This explains why etching the layer beneath the core causes a large change in the effective index of propagation ($\sim 5 \times 10^{-4}$) whereas it is only 2.9×10^{-4} when etching the very top layer. We also found that etching $> 80\%$ of a particular layer causes the loss to increase drastically because the optical mode is no longer Gaussian and confined to the core.

When studying the 3 period $Si_3N_4(n = 2)/SiO_2$ ARROW, we found that the maximum effective propagation index change is approximately 4×10^{-4}. Using higher refractive index contrast cladding materials yields a waveguide with lower loss where the optical mode is more confined to the core. Now there is less overlap between the antiresonant layers and the the fundamental mode, causing a smaller perturbation. Using more periods of antiresonant layers has the same effect because the lower loss waveguide has a smaller overlap between the cladding layers and the fundamental mode which is more tightly confined within the core.

3.1.1 Mirrors

Mirrors can be created by etching a Bragg grating into the hollow core ARROW as shown in Figure 3.1. Given that the waveguide has nonnegligible loss, the standard transfer matrix method [29] can not be used to determine the reflectivity of these gratings. We can instead use the Method of Single Expression (MSE) developed by Baghdasaryan *et al.* [30] to properly account for the absorption loss in each grating layer. Starting from the transmitting side, the field in each Bragg layer is calculated as we travel back to the illuminated side by numerically solving the coupled differential equations below.

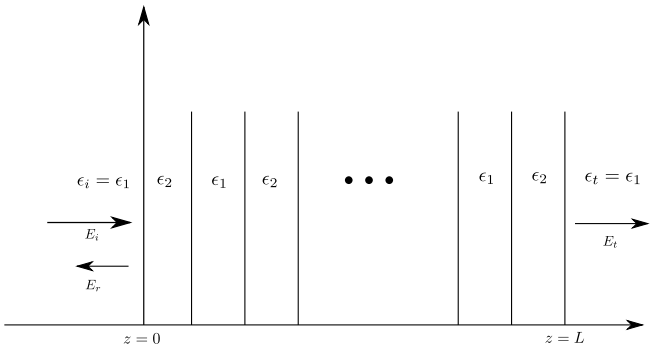

Figure 3.3: Normal incidence of a plane wave on a multilayer dielectric stack. Given the transmitted field, the incident and reflected fields can be calculated using MSE.

$$\begin{aligned}
\frac{dU(z)}{d(k_0 z)} &= Y(z) \\
\frac{dY(z)}{d(k_0 z)} &= \frac{P^2(z)}{U^3(z)} - Re\{\epsilon(z)\}U(z) \\
\frac{dP(z)}{d(k_0 z)} &= Im\{\epsilon(z)\}U^2(z)
\end{aligned}$$

where the electric field is $E(z) = U(z)e^{-iS(z)}$, $Y(z) = dU(z)/d(k_0 z)$, and the power is $P(z) = U^2(z)/[dS(z)/d(k_0 z)]$. Given a grating of length L, the initial conditions are $U(L) = 1$, $Y(L) = 0$, and $P(L) = \sqrt{\epsilon_t}$ where ϵ_t is the relative permittivity of the transmitting side. The reflectivity is then given by

$$R = \left| \frac{U^2(0)\sqrt{\epsilon_i} - P(0) - jU(0)Y(0)}{U^2(0)\sqrt{\epsilon_i} + P(0) + jU(0)Y(0)} \right|^2 \tag{3.1}$$

where ϵ_i is the relative permittivity of the incident side. Now our grating can be thought of as being composed of two alternating dielectric materials n_1 (the effective index of propagation of the waveguide), and n_2 (the effective index of propagation when one of the antiresonant layers has been etched). This approximation is valid because the modes in the two regions are similarly quasi-Gaussian in the core. The corresponding Bragg thicknesses are $t_1 = \frac{\lambda}{4 \cdot Re\{n_1\}}$, and $t_2 = \frac{\lambda}{4 \cdot Re\{n_2\}}$. For the 3 period $Si_3N_4(1.74)/SiO_2$ ARROW explored in Figure 3.2, the reflectivity of the mirror is shown in Figure 3.4a for various etched layer cases. The etch depth is chosen such that it creates the highest effective propagation index contrast relative to the original waveguide. The reflectivity spectrum of the best mirror created by etching the layer beneath the core is shown in Figure 3.4b.

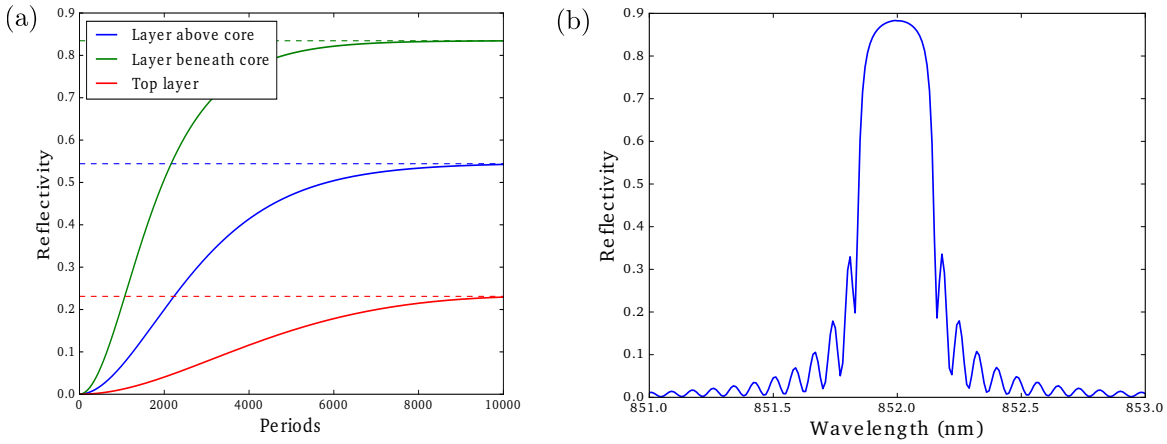

Figure 3.4: (a) Mirror reflectivites of the possible ARROW Bragg gratings. Dotted lines denote the maximum reflectivity for a particular grating. The relative etch depths for the layer above the core, layer beneath the core, and top layer are 74%, 70%, and 68% respectively. (b) Using MSE with plane wave incidence, we obtain the reflectivity spectrum of a 10000 period Bragg mirror created by periodically etching the antiresonant layer beneath the core. The etch depth is 70% of this layer, which creates an effective propagation index contrast of 5×10^{-4} with a 8% increase in loss.

We find that implementing the grating in the antiresonant layer beneath the core yields

the highest reflectivity ($\sim 84\%$) mirror. The next best mirror with $\sim 55\%$ reflectivity can be implemented using the layer above the core, while using the top layer yields a poor mirror ($\sim 23\%$) due to its low effective index contrast. Notice that with a typical lossless Bragg grating, its reflectivity increases with higher refractive contrast materials and larger number of periods. Regardless of the refractive index contrast, the reflectivity approaches 1 as we add more periods. However, with our ARROW gratings the upper bound on the reflectivity is less than 1 due to the presence of absorption loss.

3.1.2 Cavities

Cavities have typically been used to enhance the electric field inside a medium. A linear Fabry-Perot cavity consists of a spacer region surrounded by two mirrors. The interference between the multiple forward and backward propagating waves creates a standing wave inside the spacer where the electrical field intensity can be increased. This effectively enhances the electric field of a single photon over the longitudinal modal length which increases the probability of single atom-photon interaction. Here we look at creating a distributed Bragg reflector (DBR) cavity using a half wavelength spacer region as shown in Figure 3.5c. Given the high losses of the ARROWs, the shortest possible spacer length was chosen. Using MSE, we look at the 3 period $Si_3N_4(1.74)/SiO_2$ ARROW analyzed in Figure 3.4. Figure 3.5a shows how the the number of periods in the mirror affects the field intensity enhancement. The electric field intensity distribution using the optimal number of Bragg mirror periods is shown in Figure 3.5b.

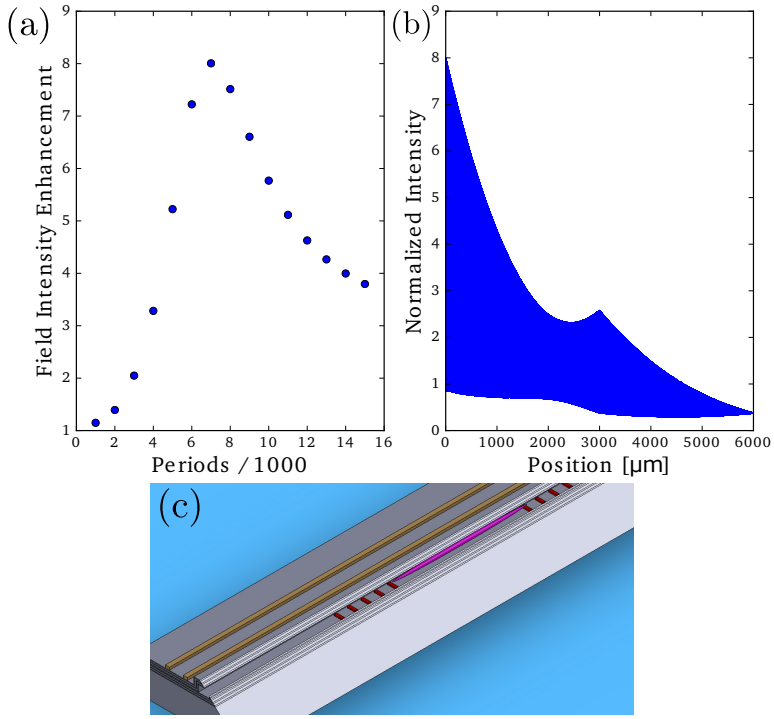

Figure 3.5: (a) Field intensity enhancement in a cavity using a half wavelength spacer for various grating mirror periods. (b) Electric field intensity distribution throughout the cavity with 7000 period Bragg mirrors. z = 0 marks the start of the cavity with the field being 1. (c) Schematic of proposed ARROW waveguide cavity with integrated Bragg grating mirrors.

We find that there is an optimal number of Bragg mirror periods to maximize the field intensity enhancement. While adding more periods can lead to a higher field intensity, adding too many increases the amount of absorption loss inside which lowers this enhancement. In a typical cavity, the field is enhanced in the spacer region. However with our proposed ARROW cavity, the field intensity is actually enhanced in the mirror region near the incident light. The high propagation loss of the ARROW prevents the field from building up inside the spacer because the waves decay quickly in the Bragg layers. Nonetheless, we find that there is moderate field intensity enhancement (~ 8) using these lossy ARROW waveguides. We note that the field monotonically decays once it enters this "cavity" and that the power is distributed throughout, unlike a traditional cavity where the power is

mostly confined to the spacer region.

3.2 Metasurface cavities

Another approach to create integrated cavities is to attach highly reflective ($> 99\%$) photonic crystal membranes to both ends of a hollow core ARROW waveguide. These metasurfaces are comprised of a thin dielectric film with a pattern of holes which can cause light that is incident perpendicular to the plane of the membrane to be completely reflected [31]. The main parameters used to design these mirrors are the refractive index of the dielectric, radius of the holes, spacing between the holes, and the thickness of the membrane. The mirrors can be made polarization selective by changing the circular holes to elliptical ones. Using these dielectric metasurface mirrors allows for loading of atomic ensembles into the waveguide through the porous membrane.

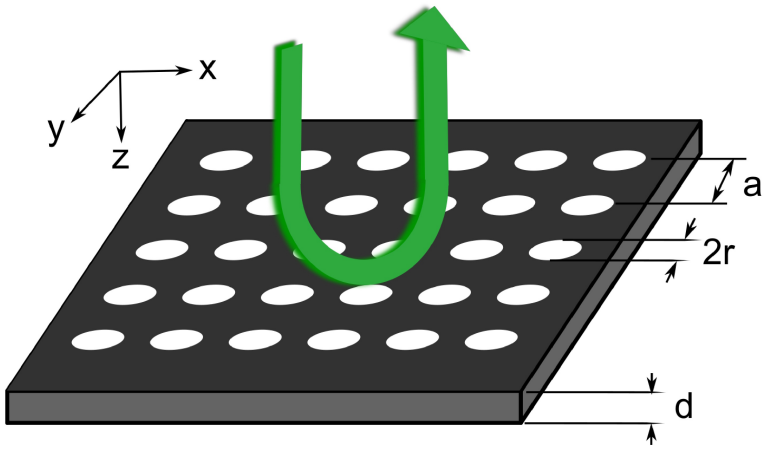

Figure 3.6: A photonic crystal membrane may act as a mirror for light that is incident perpendicular to the plane.

The strength of light-matter interaction inside the cavity can be characterized by three parameters: the photon loss rate κ out of the cavity (determined by the waveguide loss), the atomic spontaneous emission rate γ into a non-cavity mode, and the coupling strength between the cavity mode and the atom g. The coupling strength is given by

$$g = \frac{\mu}{\hbar}\sqrt{\frac{\hbar\omega}{2\epsilon_M V_{mode}}} \tag{3.2}$$

where μ is the atomic transition dipole moment, and ϵ_M is the permittivity where the field intensity is highest. The mode volume is given by

$$\begin{aligned} V_{mode} &= \frac{\iiint_V \epsilon |E|^2 \, dV}{\max\{\epsilon |E|^2\}} \\ &= A_{mode} L_{eff} \end{aligned}$$

where A_{mode} is the waveguide mode area, and L_{eff} is the effective mode length of the standing wave in the cavity. Unlike the previous DBR cavity using ARROW Bragg gratings where the power is distributed throughout the mirror regions and the spacer, here the power is mostly concentrated in the waveguide spacer region due to the use of flat mirrors. Taking into account the waveguide loss α and mirror reflectivity R, the quality factor of the cavity is given by

$$Q = \frac{\omega L n}{c(\alpha L - \ln R)} \tag{3.3}$$

where c is the speed of light, L is the waveguide length, and $n \sim 1$ is the index of propagation in the waveguide. The radiative decay rate out of the cavity is then $\kappa = \omega/Q$.

There are two regimes of light-matter interaction that we are interested in. There is the high cooperativity regime ($g^2 > \kappa\gamma$) where the presence of a single atom changes the transmission properties of the cavity. There is also the strong coupling regime ($g > \kappa, \gamma$) where a single photon coherently interacts with a single atom which undergoes multiple Rabi oscillations. These two regimes are pivotal in cavity QED experiments [32, 33]. The high cooperativity regime is easier to attain because the coupling strength does not have to exceed both the atomic decay rate and the cavity decay rate simultaenously. In the high cooperativity regime it is still possible to observe nonlinear quantum phenomena such as polariton induced cavity mode splitting and electromagnetically induced transparency (EIT). Given the fairly large waveguide losses, the strong coupling regime is not attainable with ARROWs because photon leakage rate out of the cavity is much greater than the coupling strength between an atom and a single photon. Figure 3.7a shows the cooperativity ($g^2/\kappa\gamma$) of the cavities formed using a 3 period $SiN(1.74)/SiO_2$ hollow core ARROW with cesium atoms loaded inside.

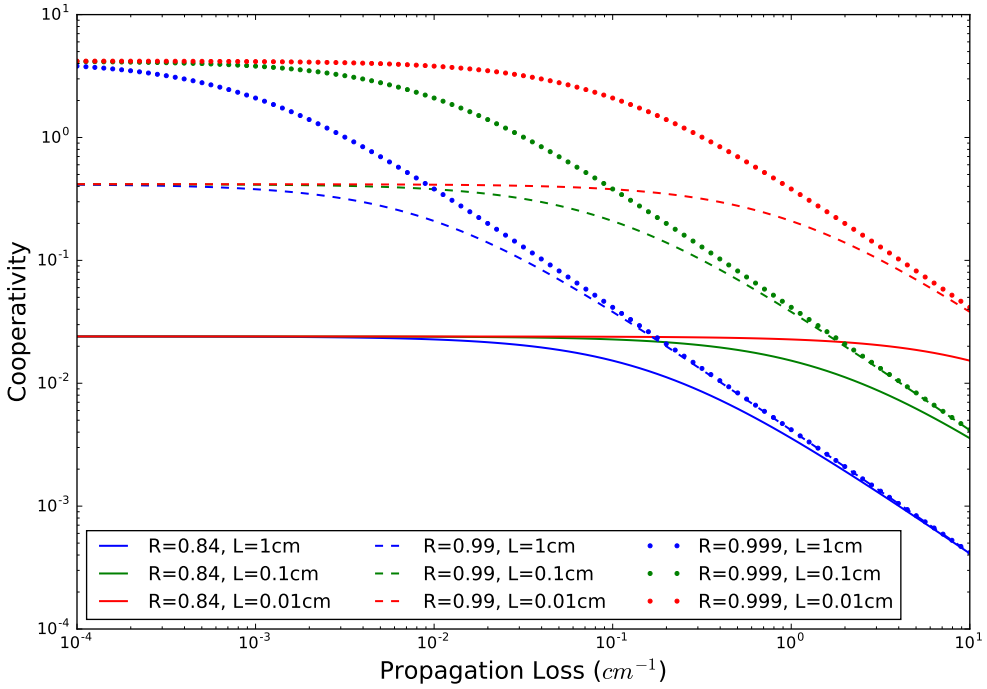

Figure 3.7: Cooperativity of hollow core ARROW ($A_{mode} = 18\mu m^2$) cavity formed using dielectric metasurface mirrors for various waveguide lengths and mirror reflectivities.

Unfortunately we find that when using a hollow core ARROW, even with highly reflective mirrors the waveguide loss required to achieve the high cooperativity regime is orders of magnitude below what has been reported theoretically or experimentally. When using the best Bragg mirror ($R \sim 84\%$) from Figure 3.4a, the upper limit on the cooperativity is $\sim 2.5 \times 10^{-2}$, far below what is required. Here we note that the cooperativity depends only on the mirror reflectivity when the waveguide loss is low, and on the cavity length when the waveguide loss is high which is expected given Equations 3.3 and 3.2.

Chapter 4

Single photon extraction

4.1 Motivation

Extracting a single photon from an optical pulse is one of most fundamental operations can be performed on it [10]. It has important applications in quantum information processing [34, 35, 36]. Single photon subtraction has typically been done using a low reflectivity beam splitter [11]. However, this method is not very deterministic and depends strongly on the number of input photons. Rosenblum *et al.* have recently demonstrated deterministic single photon extraction from an optical pulse using a 3 level atom atom evanescently coupled to a microsphere resonator [5]. This particular implementation uses an atom with two ground states where the transitions have opposite spins (Figure 4.1).

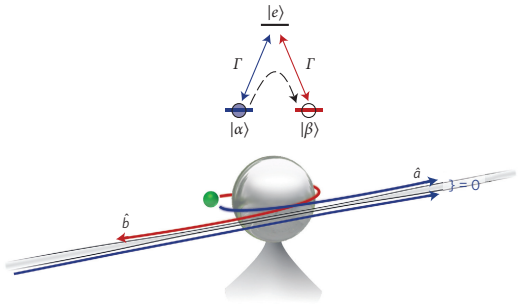

Figure 4.1: Schematic of single photon extraction using single-photon Raman interaction (SPRINT) [5]. Γ is the spontaneous emission rate into a resonator mode.

Here the atom is initially in first ground state $|\alpha\rangle$. The incoming photons from the fibre couple into the counter-clockwise propagating mode of the resonator. The resonator modes are TM, hence the clockwise and counter-clockwise travelling modes have opposite handed circular polarizations of the electric field in the plane of propagation. Given this, the two atomic transitions couple to counter propagating modes. Once the atom is excited, the waveguide transmission and radiative atomic transition into $|\alpha\rangle$ is blocked due to destructive interference. It will eventually undergo transition to the second ground state $|\beta\rangle$ and emit a clockwise propagating photon into the resonator. This photon then couples into the backward propagating waveguide mode and is collected. Once atom is in the second ground state, it no longer interacts with the incoming photons which do not have the right spin and the waveguide becomes transparent once again. However for this method to work, the coupling between the fibre and resonator must be tuned such that destructive interference occurs between the waveguide transmission and atom emission so that the atom preferentially goes into the second ground state. Here we propose using a similar Λ system coupled coupled to a chiral waveguide to perform deterministic single photon extraction.

Typically a quantum emitter couples equally to the counter-propagating modes of a waveguide. However this symmetry can be broken in certain nanophotonic structures such as the glide plane waveguide (GPW) [12], or a gold nanoparticle evanescently coupled to the TM mode of a nanofibre [37]. In each case the helicity of the atomic transition determines the photon's direction of propagation in the waveguide (ie. photons of opposite handed circular polarizations propagate in opposite directions). If a 3 level system were to be coupled to the waveguide, the two transitions would couple to counter propagating mode as shown in Figure 4.2

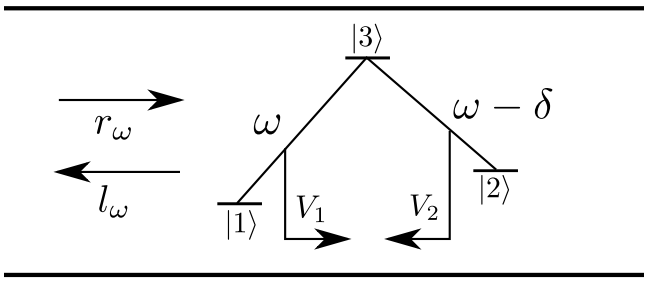

Figure 4.2: Overview of a 3 level system coupled to a chiral waveguide.

The basic principle is that given some input photons from the left with the emitter initially in the $|1\rangle$ state, it will excite to the $|3\rangle$ state. Subsequent emission of a photon

via the $|3\rangle \rightarrow |1\rangle$ transition is blocked due to destructive interference with the incoming photons. This causes the transmission of the waveguide to drop until the emitter transitions to the $|2\rangle$ state and emits a left propagating photon which can then be collected. Once this happens, the emitter no longer interacts with the incoming photons because they do not couple to the $|2\rangle \rightarrow |3\rangle$ transition. Now we have subtracted exactly one photon from the incoming light, while letting the rest of it continue propagating forward as before. The extracted photon is redirected and can be used for other purposes.

4.2 Initial calculations

We begin with the simplest case of a continuous wave coherent input which can be solved analytically. We will utilize the input-output formalism first developed by Gardiner and Collet [38] and later extended by Fan et al. [39, 40] to study resonance fluorescence of a two level quantum emitter in a waveguide geometry. We begin with the Hamiltonian for the system shown in Figure 4.2.

$$\begin{aligned} H &= H_{waveguide} + H_{atom} + H_{interaction} \\ H_{waveguide} &= \int d\omega \omega (r_\omega^\dagger r_\omega - l_\omega^\dagger l_\omega) \\ H_{atom} &= \Omega \sigma_{33} + \delta \sigma_{22} \\ H_{interaction} &= V_1 \int d\omega (\sigma_{31} r_\omega + r_\omega^\dagger \sigma_{13}) + V_2 \int d\omega (\sigma_{32} l_\omega + l_\omega^\dagger \sigma_{23}) \end{aligned}$$

where the density operator is $\sigma_{ab} = |a\rangle \langle b|$. We obtain the Heisenberg equations of motion for the left and right waveguide mode operators.

$$\begin{aligned} \dot{r}_\omega &= -i\omega r_\omega - iV_1 \sigma_{13} \\ \dot{l}_\omega &= i\omega r_\omega - iV_2 \sigma_{23} \end{aligned}$$

The input and output operator of these modes are defined by

$$
\begin{aligned}
r_{in}(t) &= \frac{1}{\sqrt{2\pi}} \int d\omega r_{\omega}(t_0) e^{-i\omega(t-t_0)} \\
r_{out}(t) &= \frac{1}{\sqrt{2\pi}} \int d\omega r_{\omega}(t_1) e^{-i\omega(t-t_1)} \\
l_{in}(t) &= \frac{1}{\sqrt{2\pi}} \int d\omega l_{\omega}(t_0) e^{i\omega(t-t_0)} \\
l_{out}(t) &= \frac{1}{\sqrt{2\pi}} \int d\omega l_{\omega}(t_1) e^{i\omega(t-t_1)}
\end{aligned}
$$

where at $t_0 \to \infty$ and $t_1 \to -\infty$ the input and output operators respectively are define long before and long after the interaction has taken place. Now defining two new operators ϕ_r and ϕ_l

$$
\begin{aligned}
\phi_r &= \frac{1}{\sqrt{2\pi}} \int d\omega r_{\omega}(t) \\
&= r_{in} - i\sqrt{\frac{2}{\pi}} V_1 \sigma_{13} \\
&= r_{out} + i\sqrt{\frac{2}{\pi}} V_1 \sigma_{13} \\
\phi_l &= \frac{1}{\sqrt{2\pi}} \int d\omega l_{\omega}(t) \\
&= l_{in} - i\sqrt{\frac{2}{\pi}} V_2 \sigma_{23} \\
&= l_{out} + i\sqrt{\frac{2}{\pi}} V_2 \sigma_{23}
\end{aligned}
$$

we can combine these relations to arrive at the input output formalism of the waveguide.

$$
\begin{aligned}
r_{out} &= r_{in} - i\sqrt{2\pi} V_1 \sigma_{13} \\
l_{out} &= l_{in} - i\sqrt{2\pi} V_2 \sigma_{23}
\end{aligned}
$$

Now applying the Heisenberg equation of motion to the various density operators, and adding the Lindblad superoperator to account for the emitter's spontaneous emission rate ($2\gamma_1$ for $|3\rangle \to |1\rangle$ transition and $2\gamma_2$ for $|3\rangle \to |2\rangle$) into a non-waveguide mode, we have

$$\begin{aligned}\dot{\rho} &= -i[H,\rho] + L(\sqrt{2\gamma_1}\sigma_{13})\rho + L(\sqrt{2\gamma_2}\sigma_{23})\rho \\ &= -i[H,\rho] + 2\gamma_1\sigma_{13}\rho\sigma_{31} + 2\gamma_2\sigma_{23}\rho\sigma_{32} - (\gamma_1+\gamma_2)(\sigma_{33}\rho + \rho\sigma_{33})\end{aligned}$$

Finally, we arrive at the Bloch equations for this system.

$$\begin{aligned}
\dot{\sigma}_{13} &= i\sqrt{2\pi}V_1(\sigma_{33}-\sigma_{11})r_{in} - i\sqrt{2\pi}V_2\sigma_{12}l_{in} - (\pi(V_1^2+V_2^2)+\gamma_1+\gamma_2+i\Omega)\sigma_{13} \\
\dot{\sigma}_{31} &= -i\sqrt{2\pi}V_1r_{in}^\dagger(\sigma_{33}-\sigma_{11}) + i\sqrt{2\pi}V_2l_{in}^\dagger\sigma_{21} - (\pi(V_1^2+V_2^2)+\gamma_1+\gamma_2-i\Omega)\sigma_{31} \\
\dot{\sigma}_{23} &= i\sqrt{2\pi}V_2(\sigma_{33}-\sigma_{22})l_{in} - i\sqrt{2\pi}V_1\sigma_{21}r_{in} - (\pi(V_1^2+V_2^2)+\gamma_1+\gamma_2+i(\Omega-\delta))\sigma_{23} \\
\dot{\sigma}_{32} &= -i\sqrt{2\pi}V_2l_{in}^\dagger(\sigma_{33}-\sigma_{22}) + i\sqrt{2\pi}V_1r_{in}^\dagger\sigma_{12} - (\pi(V_1^2+V_2^2)+\gamma_1+\gamma_2-i(\Omega-\delta))\sigma_{32} \\
\dot{\sigma}_{33} &= -i\sqrt{2\pi}V_1(\sigma_{31}r_{in} - r_{in}^\dagger\sigma_{13}) - i\sqrt{2\pi}V_2(\sigma_{32}l_{in} - l_{in}^\dagger\sigma_{23}) - 2(\pi(V_1^2+V_2^2)+\gamma_1+\gamma_2)\sigma_{33} \\
\dot{\sigma}_{11} &= i\sqrt{2\pi}V_1(\sigma_{31}r_{in} - r_{in}^\dagger\sigma_{13}) + 2(\pi V_1^2+\gamma_1)\sigma_{33} \\
\dot{\sigma}_{22} &= i\sqrt{2\pi}V_2(\sigma_{32}l_{in} - l_{in}^\dagger\sigma_{23}) + 2(\pi V_2^2+\gamma_2)\sigma_{33} \\
\dot{\sigma}_{12} &= i\sqrt{2\pi}V_1\sigma_{32}r_{in} - i\sqrt{2\pi}V_2l_{in}^\dagger\sigma_{13} - i\delta\sigma_{12} \\
\dot{\sigma}_{21} &= -i\sqrt{2\pi}V_1r_{in}^\dagger\sigma_{23} + i\sqrt{2\pi}V_2\sigma_{31}l_{in} + i\delta\sigma_{21}
\end{aligned}$$

Now given a continuous wave coherent input state $|\alpha_\omega\rangle$ at frequency ω coming from the left where

$$r_{in}(t)\,|\alpha_\omega\rangle = \frac{\alpha}{\sqrt{2\pi}}e^{-i\omega t}\,|\alpha_\omega\rangle \tag{4.1}$$

we can find the expectation values of the Bloch operators. Taking these values into the the rotating frame ($\sigma_{13} \to \sigma_{13}e^{-i\omega t}$, $\sigma_{23} \to \sigma_{23}e^{-i\omega t}$), we have

$$
\begin{aligned}
\langle\dot{\sigma}_{13}\rangle &= iV_1\alpha(\langle\sigma_{33}\rangle - \langle\sigma_{11}\rangle) - (\pi(V_1^2+V_2^2)+\gamma_1+\gamma_2+i(\Omega-\omega))\langle\sigma_{13}\rangle \\
\langle\dot{\sigma}_{31}\rangle &= -iV_1\bar{\alpha}(\langle\sigma_{33}\rangle - \langle\sigma_{11}\rangle) - (\pi(V_1^2+V_2^2)+\gamma_1+\gamma_2-i(\Omega-\omega))\langle\sigma_{31}\rangle \\
\langle\dot{\sigma}_{23}\rangle &= -iV_1\alpha\langle\sigma_{21}\rangle - (\pi(V_1^2+V_2^2)+\gamma_1+\gamma_2+i(\Omega-\omega-\delta))\langle\sigma_{23}\rangle \\
\langle\dot{\sigma}_{32}\rangle &= iV_1\bar{\alpha}\langle\sigma_{12}\rangle - (\pi(V_1^2+V_2^2)+\gamma_1+\gamma_2-i(\Omega-\omega-\delta))\langle\sigma_{32}\rangle \\
\langle\dot{\sigma}_{33}\rangle &= -iV_1(\langle\sigma_{31}\rangle\alpha - \bar{\alpha}\langle\sigma_{13}\rangle) - 2(\pi(V_1^2+V_2^2)+\gamma_1+\gamma_2)\langle\sigma_{33}\rangle \\
\langle\dot{\sigma}_{11}\rangle &= iV_1(\langle\sigma_{31}\rangle\alpha - \bar{\alpha}\langle\sigma_{13}\rangle) + 2(\pi V_1^2+\gamma_1)\langle\sigma_{33}\rangle \\
\langle\dot{\sigma}_{22}\rangle &= 2(\pi V_2^2+\gamma_2)\langle\sigma_{33}\rangle \\
\langle\dot{\sigma}_{12}\rangle &= iV_1\alpha\langle\sigma_{32}\rangle - i\delta\langle\sigma_{12}\rangle \\
\langle\dot{\sigma}_{21}\rangle &= -iV_1\bar{\alpha}\langle\sigma_{23}\rangle + i\delta\langle\sigma_{21}\rangle
\end{aligned}
$$

Next we can take the Laplace transform of the equations above with the initial condition that the emitter is in the first ground state ($\langle\sigma_{ab}(0)\rangle = 0$ with the exception of $\langle\sigma_{11}(0)\rangle = 1$) and use the Laplace identity ($\mathcal{L}\{\langle\dot{\sigma}_{ab}\rangle\} = s\mathcal{L}\{\langle\sigma_{ab}\rangle\} - \langle\sigma_{ab}(0)\rangle$). Then after solving we have

$$
\mathcal{L}\{\langle\sigma_{13}\rangle\} = \frac{-iV_1\alpha(s+2(\pi(V_1^2+V_2^2)+\gamma_1+\gamma_2))(s+\pi(V_1^2+V_2^2)+\gamma_1+\gamma_2-i(\Omega-\omega))}{s(s+2(\pi(V_1^2+V_2^2)+\gamma_1+\gamma_2))((s+\pi(V_1^2+V_2^2)+\gamma_1+\gamma_2)^2+(\Omega-\omega)^2)+4V_1^2|\alpha|^2(s+\pi V_2^2+\gamma_2)(s+\pi(V_1^2+V_2^2)+\gamma_1+\gamma_2)}
$$

$$
\mathcal{L}\{\langle\sigma_{31}\rangle\} = \frac{iV_1\bar{\alpha}(s+2(\pi(V_1^2+V_2^2)+\gamma_1+\gamma_2))(s+\pi(V_1^2+V_2^2)+\gamma_1+\gamma_2+i(\Omega-\omega))}{s(s+2(\pi(V_1^2+V_2^2)+\gamma_1+\gamma_2))((s+\pi(V_1^2+V_2^2)+\gamma_1+\gamma_2)^2+(\Omega-\omega)^2)+4V_1^2|\alpha|^2(s+\pi V_2^2+\gamma_2)(s+\pi(V_1^2+V_2^2)+\gamma_1+\gamma_2)}
$$

$$
\mathcal{L}\{\langle\sigma_{33}\rangle\} = \frac{2V_1^2|\alpha|^2(s+\pi(V_1^2+V_2^2)+\gamma_1+\gamma_2)}{s(s+2(\pi(V_1^2+V_2^2)+\gamma_1+\gamma_2))((s+\pi(V_1^2+V_2^2)+\gamma_1+\gamma_2)^2+(\Omega-\omega)^2)+4V_1^2|\alpha|^2(s+\pi V_2^2+\gamma_2)(s+\pi(V_1^2+V_2^2)+\gamma_1+\gamma_2)}
$$

Now the reflected field is given by

$$
\begin{aligned}
\left\langle l_{out}^\dagger l_{out}\right\rangle &= \left\langle l_{in}^\dagger l_{in}\right\rangle + iV_2\bar{\alpha}\langle\sigma_{23}\rangle - iV_2\alpha\langle\sigma_{32}\rangle + 2\pi V_2^2\langle\sigma_{33}\rangle \\
&= 2\pi V_2^2\langle\sigma_{33}\rangle
\end{aligned}
$$

The probability of detecting a single photon at the left output is given by

$$
\begin{aligned}
P_l &= \int_0^\infty \left\langle l_{out}^\dagger l_{out}\right\rangle dt \\
&= \int_0^\infty 2\pi V_2^2\langle\sigma_{33}\rangle\, dt
\end{aligned}
$$

Now applying the Laplace identity $\left(\mathcal{L}\{\int_0^t \langle\sigma_{ab}\rangle\, dt\} = \frac{\mathcal{L}\{\langle\sigma_{ab}\rangle\}}{s}\right)$, and the final value theorem ($\lim_{t\to\infty}\langle\sigma_{ab}(t)\rangle = \lim_{s\to 0} s\mathcal{L}\{\langle\sigma_{ab}\rangle\}$), we have that

$$\begin{aligned} P_l &= 2\pi V_2^2 \lim_{s\to 0} s\frac{\mathcal{L}\{\langle\sigma_{33}\rangle\}}{s} \\ &= 2\pi V_2^2 \lim_{s\to 0} \mathcal{L}\{\langle\sigma_{33}\rangle\} \\ &= \frac{\pi V_2^2}{\pi V_2^2 + \gamma_2} \\ &= 1 - \frac{\gamma_2}{\pi V_2^2 + \gamma_2} \end{aligned}$$

We find that the probability of detecting a single photon on the left side depends only on the rate of emitter decay from $|3\rangle \to |2\rangle$ and the emission rate into the left propagating mode of the waveguide ($P_l \sim 1$ for $\gamma_2 \ll V_2^2$). Now we need to take a look at the outgoing beam to find the number of photons subtracted.

$$\left\langle r_{out}^\dagger r_{out} \right\rangle = \left\langle r_{in}^\dagger r_{in} \right\rangle + iV_1(\alpha\langle\sigma_{31}\rangle - \bar{\alpha}\langle\sigma_{13}\rangle) + 2\pi V_1^2\langle\sigma_{33}\rangle$$

$$\begin{aligned} N_{subtracted} &= \int_0^\infty dt \left(\left\langle r_{in}^\dagger r_{in} \right\rangle - \left\langle r_{out}^\dagger r_{out} \right\rangle\right) \\ &= \lim_{s\to 0} iV_1(\alpha\mathcal{L}\{\langle\sigma_{31}\rangle\} - \bar{\alpha}\mathcal{L}\{\langle\sigma_{13}\rangle\}) + 2\pi V_1^2\mathcal{L}\{\langle\sigma_{33}\rangle\} \\ &= 1 + \frac{\gamma_1}{\pi V_2^2 + \gamma_2} \end{aligned}$$

We find that slightly more than one photon is subtracted from the input due to the excited emitter state decay from $|3\rangle \to |1\rangle$ via a non-waveguide mode while it has not transitioned to the noninteracting $|2\rangle$ state. We do not always collect the extracted photon at the left output due to γ_2. The number of photons subtracted is independent of both the coupling between the right propagating waveguide mode and the $|1\rangle \to |3\rangle$ transition and the rate of incoming photons ($|\alpha|^2$).

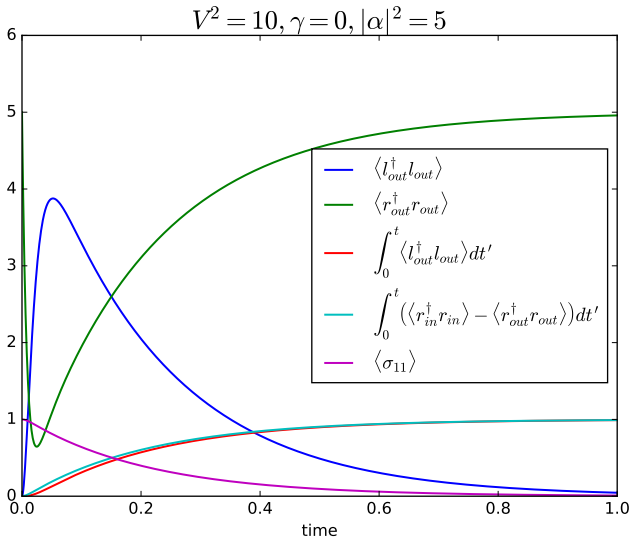

Figure 4.3: Output values of the various operators given a continuous wave coherent input.

Figure 4.3 shows the expectation values of the various observables for a set of system parameters. When the rate of incoming photons is low, there is a greater drop in the transmission of the waveguide until a photon is subtracted. This is because the emitted photon from the $|3\rangle \rightarrow |1\rangle$ transition has a longer effective interaction time with the incoming photons with which it destructively interferes. Also, the time it takes to extract a single photon increases for weaker coupling strengths between the waveguide modes and the 3 level Λ emitter, as well as a lower rate of incoming photons. A weaker coupling strength implies a longer lifetime in the excited state.

4.3 Coherent pulse calculations

The previous was straightforward and educational, but for practical purposes we now take a look at how successful the photon subtraction operation is if the input is actually a coherent pulse containing a finite number of photons. The initial calculations were akin to a single photon source because we do not gain any information about the continuous wave output. Here we will consider the case of a coherent Gaussian like input wave-packet [41]. The input state is defined as

$$|\psi_{in}\rangle = e^{r_{in,\alpha} - r^{\dagger}_{in,\alpha}} |0\rangle \tag{4.2}$$

where α satisfies

$$\int |\alpha(t)|^2 dt = \int |\alpha(\omega)|^2 d\omega = \langle n \rangle \tag{4.3}$$

with $\langle n \rangle$ being the number of photons in the wave-packet. Applying the input operators to this state, we get that

$$\begin{aligned} r_{in}(t) |\psi_{in}\rangle &= \alpha(t) |\psi_{in}\rangle \\ r_{in}(\omega) |\psi_{in}\rangle &= \alpha(\omega) |\psi_{in}\rangle \end{aligned}$$

These input operators are related by the Fourier transform

$$\begin{aligned} r_{in}(t) &= \frac{1}{\sqrt{2\pi}} \int d\omega r_{in}(\omega) e^{i\omega t} \\ r_{in}(\omega) &= \frac{1}{\sqrt{2\pi}} \int dt r_{in}(t) e^{-i\omega t} \end{aligned}$$

and satisfy the commutation relations

$$\begin{aligned} [r_{in}(t), r^{\dagger}_{in}(t')] &= \delta(t - t') \\ [r_{in}(\omega), r^{\dagger}_{in}(\omega')] &= \delta(\omega - \omega') \end{aligned}$$

Now choosing a Gaussian wave-packet with width τ, we can define

$$\alpha(t) = \frac{\sqrt{2 \langle n \rangle}}{\sqrt[4]{\pi \tau^2}} e^{-2t^2/\tau^2} \tag{4.4}$$

The expectation values of the Bloch equations in the rotating frame become

$$\langle \dot{\sigma}_{13} \rangle = i\sqrt{2\pi} V_1 \alpha(t)(\langle \sigma_{33} \rangle - \langle \sigma_{11} \rangle) - (\pi(V_1^2 + V_2^2) + \gamma_1 + \gamma_2 + i(\Omega - \omega)) \langle \sigma_{13} \rangle$$
$$\langle \dot{\sigma}_{31} \rangle = -i\sqrt{2\pi} V_1 \bar{\alpha}(t)(\langle \sigma_{33} \rangle - \langle \sigma_{11} \rangle) - (\pi(V_1^2 + V_2^2) + \gamma_1 + \gamma_2 - i(\Omega - \omega)) \langle \sigma_{31} \rangle$$
$$\langle \dot{\sigma}_{23} \rangle = -i\sqrt{2\pi} V_1 \alpha(t) \langle \sigma_{21} \rangle - (\pi(V_1^2 + V_2^2) + \gamma_1 + \gamma_2 + i(\Omega - \omega - \delta)) \langle \sigma_{23} \rangle$$
$$\langle \dot{\sigma}_{32} \rangle = i\sqrt{2\pi} V_1 \bar{\alpha}(t) \langle \sigma_{12} \rangle - (\pi(V_1^2 + V_2^2) + \gamma_1 + \gamma_2 - i(\Omega - \omega - \delta)) \langle \sigma_{32} \rangle$$
$$\langle \dot{\sigma}_{33} \rangle = -i\sqrt{2\pi} V_1 (\langle \sigma_{31} \rangle \alpha(t) - \bar{\alpha}(t) \langle \sigma_{13} \rangle) - 2(\pi(V_1^2 + V_2^2) + \gamma_1 + \gamma_2) \langle \sigma_{33} \rangle$$
$$\langle \dot{\sigma}_{11} \rangle = i\sqrt{2\pi} V_1 (\langle \sigma_{31} \rangle \alpha(t) - \bar{\alpha}(t) \langle \sigma_{13} \rangle) + 2(\pi V_1^2 + \gamma_1) \langle \sigma_{33} \rangle$$
$$\langle \dot{\sigma}_{22} \rangle = 2(\pi V_2^2 + \gamma_2) \langle \sigma_{33} \rangle$$
$$\langle \dot{\sigma}_{12} \rangle = i\sqrt{2\pi} V_1 \alpha(t) \langle \sigma_{32} \rangle - i\delta \langle \sigma_{12} \rangle$$
$$\langle \dot{\sigma}_{21} \rangle = -i\sqrt{2\pi} V_1 \bar{\alpha}(t) \langle \sigma_{23} \rangle + i\delta \langle \sigma_{21} \rangle$$

with the same initial condition that the emitter is in the first ground state. We can numerically solve these equations to determine the expectation values of the various outputs as shown in Figure 4.4. We find that

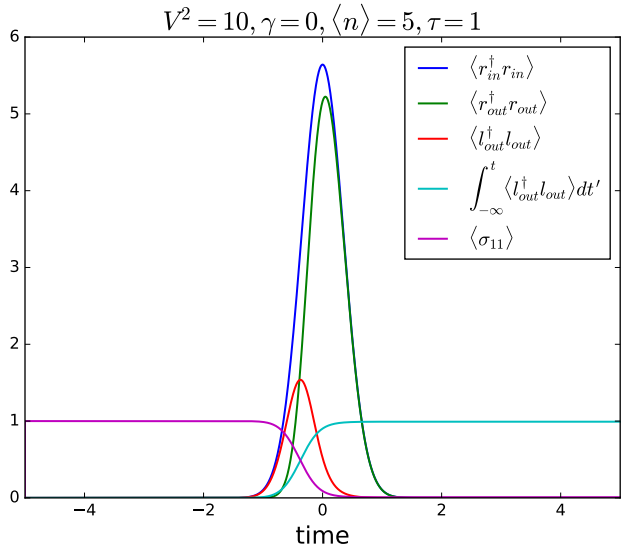

Figure 4.4: Output values for a coherent pulsed input state.

In Figure 4.3, we show that the probability of extracting a single photon is a function of

the τV^2 product. This can be thought of as the interaction product (interaction time (τ) x rate of interaction (V^2)). Compared to continuous driving, the probability of single photon extraction is always less than unity because the pulse only interacts with the emitter for a limited time (τ).

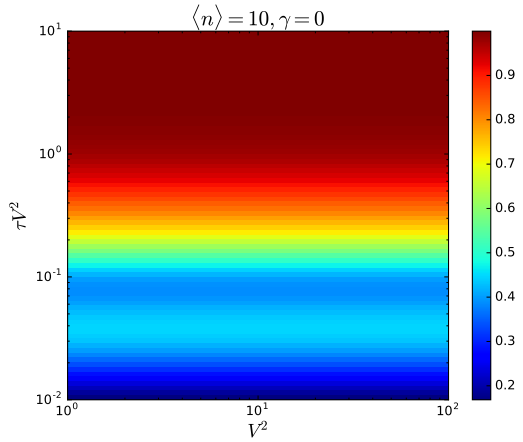

Figure 4.5: The probability of extracting a single photon is a function of the τV^2 product.

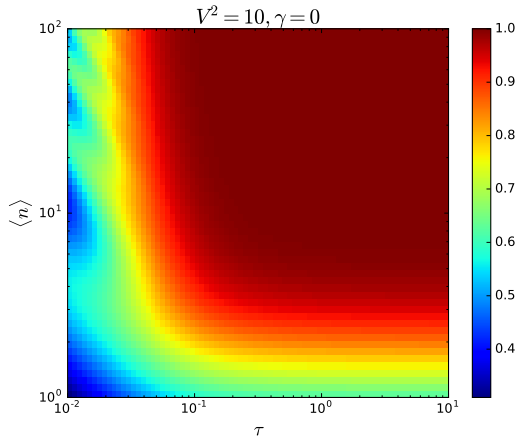

Figure 4.6: The probability of single photon extraction as a function of the interaction product and the number of photons in the input.

Therefore the probability of extracting a single photon is a function of only the interaction product and the number of photons in the input wave-packet as shown in Figure 4.6. A higher interaction product or a larger number of photons in the input wave-packet increases the probability of extracting a single photon from it.

4.4 Fock state calculations

Next, we study the single photon extraction from a Fock state pulse. Ideally we want the single photon extraction probability to be independent of the Fock state number. We begin by defining the photon wave-packet creation operator [41].

$$\begin{aligned} r^{\dagger}_{in,\alpha}(t) &= \int dt \alpha(t) r^{\dagger}_{in}(t) \\ &= \int d\omega \alpha(\omega) r^{\dagger}_{in}(\omega) \end{aligned}$$

where

$$\int |\alpha(t)|^2 dt = \int |\alpha(\omega)|^2 d\omega = 1 \tag{4.5}$$

The N photon Fock state is then defined as

$$|N_\alpha\rangle = \frac{\left(r^{\dagger}_{in,\alpha}\right)^N}{\sqrt{N!}} |0\rangle \tag{4.6}$$

which consists of N independent single photon wave-packets. Now applying the input operator $r_{in}(t)$ to this state, we have the following relation.

$$r_{in}(t) |N_\alpha\rangle = \sqrt{N}\alpha(t) |(N-1)_\alpha\rangle \tag{4.7}$$

We can similarly apply this relation to the Bloch equations to get

$$\langle N_\alpha \mid \dot{\sigma}_{13} \mid K_\alpha \rangle = i\sqrt{2\pi}V_1\sqrt{K}\alpha(t)(\langle N_\alpha \mid \sigma_{33} \mid (K-1)_\alpha \rangle - \langle N_\alpha \mid \sigma_{11} \mid (K-1)_\alpha \rangle) - (\pi(V_1^2+V_2^2)+\gamma_1+\gamma_2+i(\Omega-\omega))\langle N_\alpha \mid \sigma_{13} \mid K_\alpha \rangle$$
$$\langle N_\alpha \mid \dot{\sigma}_{31} \mid K_\alpha \rangle = -i\sqrt{2\pi}V_1\sqrt{N}\bar{\alpha}(t)(\langle (N-1)_\alpha \mid \sigma_{33} \mid K_\alpha \rangle - \langle (N-1)_\alpha \mid \sigma_{11} \mid K_\alpha \rangle) - (\pi(V_1^2+V_2^2)+\gamma_1+\gamma_2-i(\Omega-\omega))\langle N_\alpha \mid \sigma_{31} \mid K_\alpha \rangle$$
$$\langle N_\alpha \mid \dot{\sigma}_{23} \mid K_\alpha \rangle = -i\sqrt{2\pi}V_1\sqrt{K}\alpha(t)\langle N_\alpha \mid \sigma_{21} \mid (K-1)_\alpha \rangle - (\pi(V_1^2+V_2^2)+\gamma_1+\gamma_2+i(\Omega-\omega-\delta))\langle N_\alpha \mid \sigma_{23} \mid K_\alpha \rangle$$
$$\langle N_\alpha \mid \dot{\sigma}_{32} \mid K_\alpha \rangle = i\sqrt{2\pi}V_1\sqrt{N}\bar{\alpha}(t)\langle (N-1)_\alpha \mid \sigma_{12} \mid K_\alpha \rangle - (\pi(V_1^2+V_2^2)+\gamma_1+\gamma_2-i(\Omega-\omega-\delta))\langle N_\alpha \mid \sigma_{32} \mid K_\alpha \rangle$$
$$\langle N_\alpha \mid \dot{\sigma}_{33} \mid K_\alpha \rangle = -i\sqrt{2\pi}V_1(\langle N_\alpha \mid \sigma_{31} \mid (K-1)_\alpha \rangle\sqrt{K}\alpha(t) - \sqrt{N}\bar{\alpha}(t)\langle (N-1)_\alpha \mid \sigma_{13} \mid K_\alpha \rangle) - 2(\pi(V_1^2+V_2^2)+\gamma_1+\gamma_2)\langle N_\alpha \mid \sigma_{33} \mid K_\alpha \rangle$$
$$\langle N_\alpha \mid \dot{\sigma}_{11} \mid K_\alpha \rangle = i\sqrt{2\pi}V_1(\langle N_\alpha \mid \sigma_{31} \mid (K-1)_\alpha \rangle\sqrt{K}\alpha(t) - \sqrt{N}\bar{\alpha}(t)\langle (N-1)_\alpha \sigma_{13} \mid K_\alpha \rangle) + 2(\pi V_1^2+\gamma_1)\langle N_\alpha \mid \sigma_{33} \mid K_\alpha \rangle$$
$$\langle N_\alpha \mid \dot{\sigma}_{22} \mid K_\alpha \rangle = 2(\pi V_2^2+\gamma_2)\langle N_\alpha \mid \sigma_{33} \mid K_\alpha \rangle$$
$$\langle N_\alpha \mid \dot{\sigma}_{12} \mid K_\alpha \rangle = i\sqrt{2\pi}V_1\sqrt{K}\alpha(t)\langle N_\alpha \mid \sigma_{32} \mid (K-1)_\alpha \rangle - i\delta\langle N_\alpha \mid \sigma_{12} \mid K_\alpha \rangle$$
$$\langle N_\alpha \mid \dot{\sigma}_{21} \mid K_\alpha \rangle = -i\sqrt{2\pi}V_1\sqrt{N}\bar{\alpha}(t)\langle (N-1)_\alpha \mid \sigma_{23} \mid K_\alpha \rangle + i\delta\langle N_\alpha \mid \sigma_{21} \mid K_\alpha \rangle$$

and numerically solve for the expectation values of the various operators as before. Output from a sample calculation is shown in Figure 4.7.

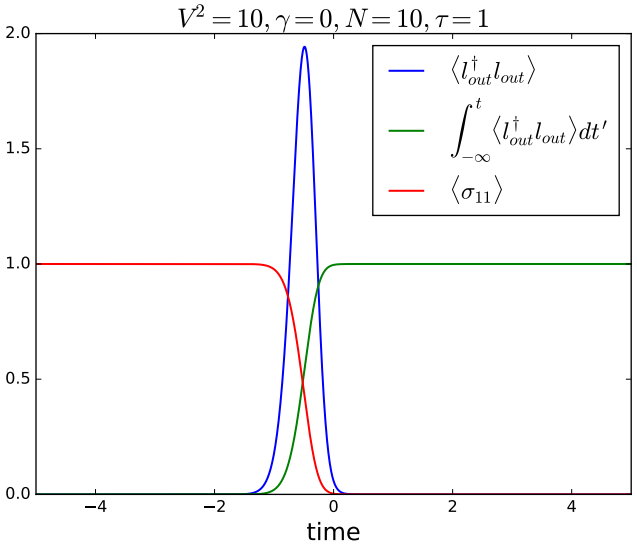

Figure 4.7: Output values for a $N = 10$ Fock state input.

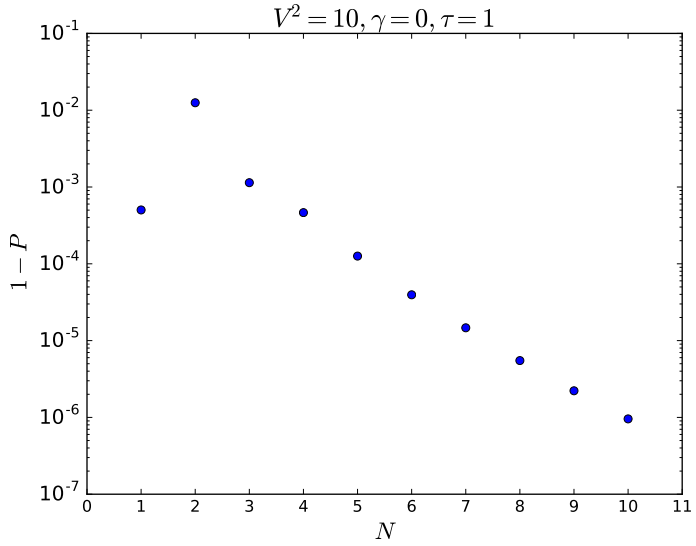

Figure 4.8: Probability of extracting a single photon from a Fock state.

We find that the probability of extracting a single photon is relatively independent of the Fock state number ($> 99\%$) for $V^2 = 10$ and $\tau = 1$. As before with the coherent pulsed input state in Figure 4.6, we found that the probability is a function of only the interaction product and the number of photons in the input (τV^2). In Figure 4.9 we compare our results for a Fock state input with those for a coherent pulsed input. We find that the probability of extraction from a Fock state is consistently greater than from a coherent state containing the same number of photons. We also find that for a particular interaction product, the success probabilities for both converge with more photons in the input as we would expect. For both Fock and coherent state inputs the probability does not seem to increase with larger interaction products ($\tau V^2 > 10$) due to some saturation effect.

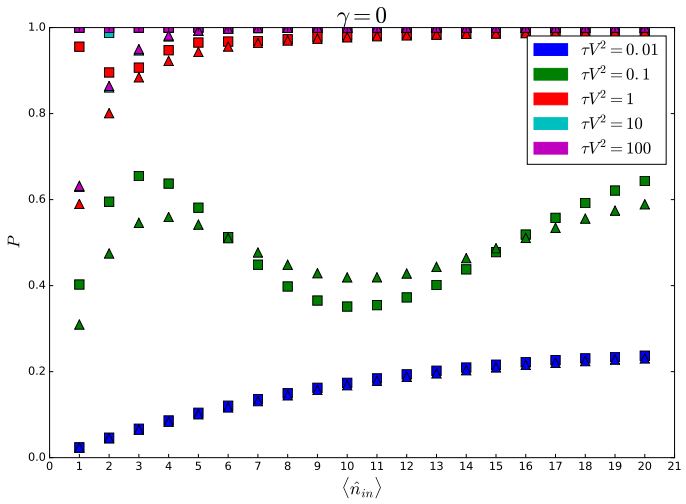

Figure 4.9: Comparison of the probability of single photon extraction from a coherent pulsed state (triangles) and a Fock state (squares).

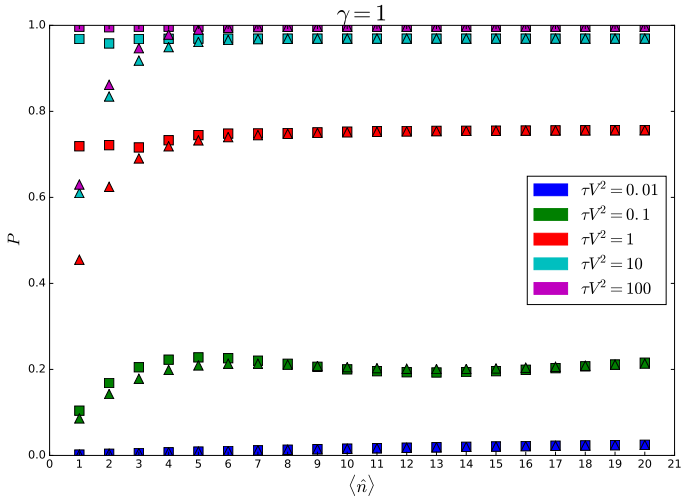

Figure 4.10: Comparison of the probability of single photon extraction from a coherent pulsed state (triangles) and a Fock state (squares) with a non-zero decay rate of the emitter.

With some emitter decay we find that the probability of extracting a single photon is reduced. Also, we observe that for higher values of the interaction product, this probability is lowered by a relatively smaller amount. Hence, there is a distinction between the $\tau V^2 = 10$ and $\tau V^2 = 100$ cases unlike in Figure 4.9.

4.5 Imperfectly directional waveguides

While in the previous calculations we assumed the waveguide to be perfectly directional (ie. opposite handed circularly polarized photons travel only in opposite directions), this is not aways the case in real systems (Figure 4.11). Specifically, the atom can emit with non-zero probability a left propagating photon after undergoing the $|3\rangle \rightarrow |1\rangle$ transition or a right propagating photon after undergoing the $|3\rangle \rightarrow |2\rangle$ transition.

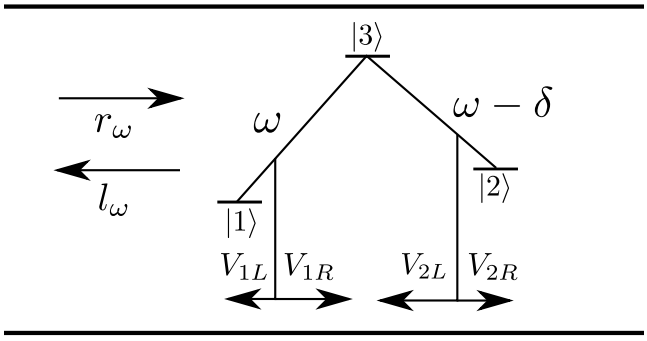

Figure 4.11: Overview of a 3 level system coupled to a non perfect chiral waveguide.

Thus, we define the directionality of the waveguide β as

$$\beta = \frac{V_{1R}^2}{V_{1R}^2 + V_{1L}^2} = \frac{V_{2L}^2}{V_{2L}^2 + V_{2R}^2} \tag{4.8}$$

where

$$V_1^2 = V_{1R}^2 + V_{1L}^2$$
$$V_2^2 = V_{2R}^2 + V_{2L}^2$$

Now we have a slightly different Hamiltonian than before

$$\begin{aligned}
H &= H_{waveguide} + H_{atom} + H_{interaction} \\
H_{waveguide} &= \int d\omega\omega(r^\dagger_{\omega_1} r_{\omega_1} + r^\dagger_{\omega_2} r_{\omega_2} - l^\dagger_{\omega_1} l_{\omega_1} - l^\dagger_{\omega_2} l_{\omega_2}) \\
H_{atom} &= \Omega\sigma_{33} + \delta\sigma_{22} \\
H_{interaction} &= V_{1R}\int d\omega(\sigma_{31} r_{\omega_1} + r^\dagger_{\omega_1}\sigma_{13}) + V_{2L}\int d\omega(\sigma_{32} l_{\omega_2} + l^\dagger_{\omega_2}\sigma_{23}) \\
&\quad + V_{1L}\int d\omega(\sigma_{31} l_{\omega_1} + l^\dagger_{\omega_1}\sigma_{13}) + V_{2R}\int d\omega(\sigma_{32} r_{\omega_2} + r^\dagger_{\omega_2}\sigma_{23})
\end{aligned}$$

Working out the Bloch equations as before, we can then apply a continuously driven coherent input state $|\alpha_{\omega_1}\rangle$ from the left where

$$r_{in}(t)\,|\alpha_{\omega_1}\rangle = \frac{\alpha}{\sqrt{2\pi}} e^{-i\omega_1 t}\,|\alpha_{\omega_1}\rangle \tag{4.9}$$

Taking the expectation values of the Bloch equations, and solving them using the Laplace transform we then arrive at the probability of detecting a single photon.

$$\begin{aligned}
P_{2L} &= \int_0^\infty dt \left\langle l^\dagger_{out,2} l_{out,2} \right\rangle = \frac{\pi\beta V_2^2}{\pi V_2^2 + \gamma_2} \\
P_{2R} &= \int_0^\infty dt \left\langle r^\dagger_{out,2} r_{out,2} \right\rangle = \frac{\pi(1-\beta) V_2^2}{\pi V_2^2 + \gamma_2} \\
P_{1L} &= \int_0^\infty dt \left\langle l^\dagger_{out,1} l_{out,1} \right\rangle = \frac{\pi(1-\beta) V_1^2}{\pi V_2^2 + \gamma_2}
\end{aligned}$$

We see that the probability of detecting the photon via the left channel is reduced by a factor of β. We also have some non-zero probability of detecting a photon from the right from the second ground state transition, and in the left from the first ground state transition due to a directionality that is less than 1. Also we can calculate the number of photons extracted from the incoming light.

$$\int_0^\infty dt \left(\left\langle r^\dagger_{in,1} r_{in,1} \right\rangle - \left\langle r^\dagger_{out,1} r_{out,1} \right\rangle \right) = 1 + \frac{\pi(1-\beta) V_1^2 + \gamma_1}{\pi V_2^2 + \gamma_2} \tag{4.10}$$

We extract more than one photon from the incoming light due to the imperfect directionality of the waveguide and the excited state decay via $|3\rangle \rightarrow |1\rangle$. We extract exactly one photon via transition to the second ground state which can only occur once. However if the emitter transitions to the first ground state and emits a photon into the waveguide, it will travel left with probability $1-\beta$, causing us to remove more photons than we desire. Next we compare the probability of extracting a single photon via the left channel when the input is a coherent pulsed state or a Fock state.

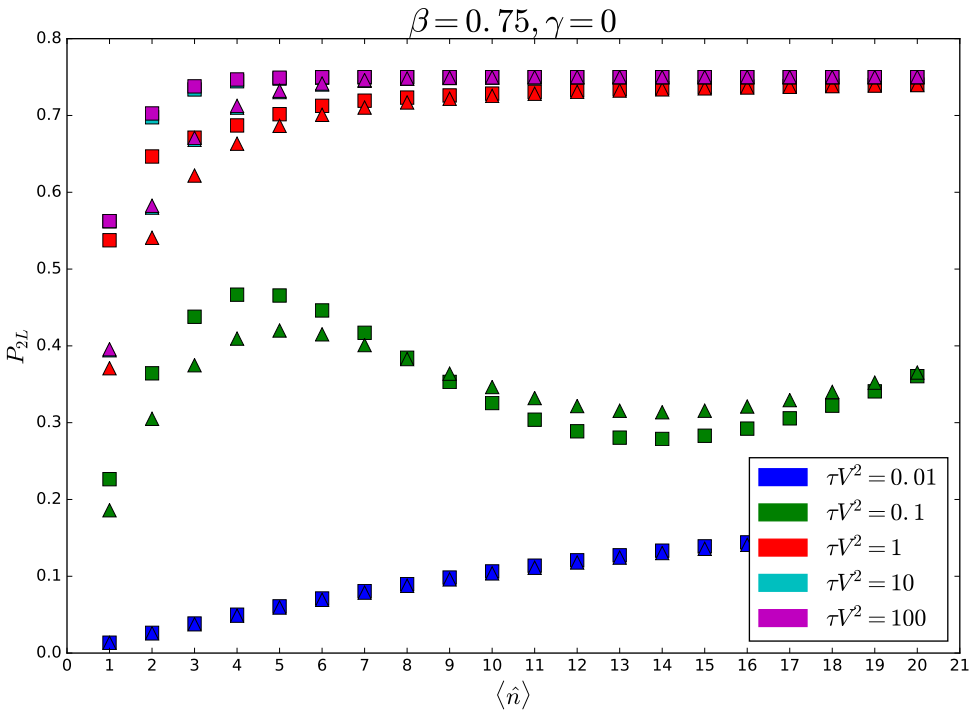

Figure 4.12: Comparison of the probability of single photon extraction via the left channel from a coherent pulsed state (triangles) and a Fock state (squares) with $\beta = 0.75$.

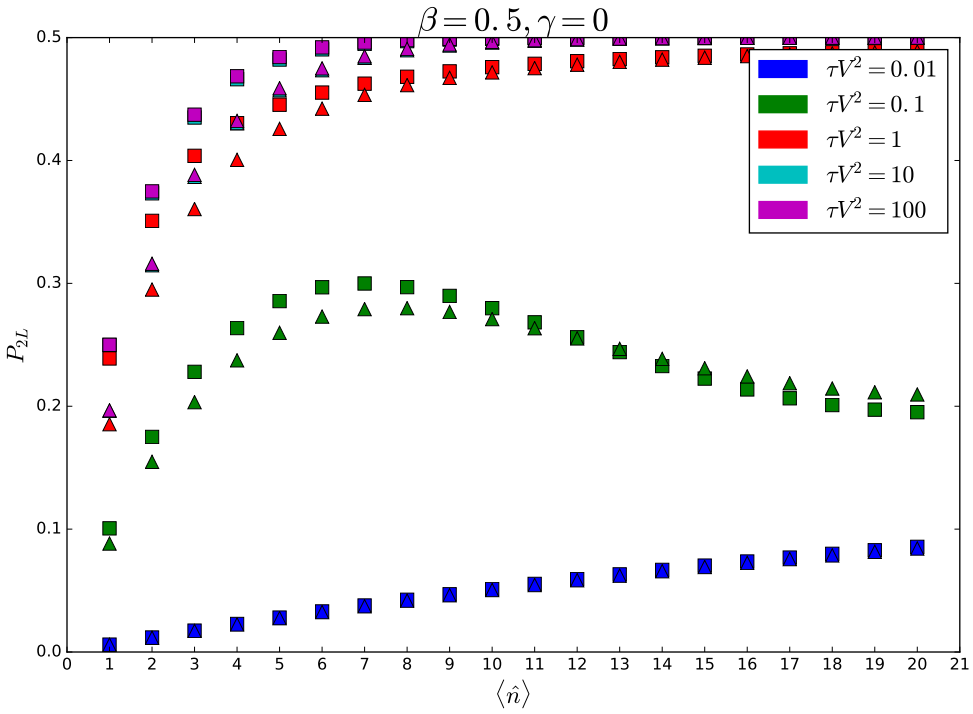

Figure 4.13: Comparison of the probability of single photon extraction via the left channel from a coherent pulsed state (triangles) and a Fock state (squares) using a nondirectional waveguide.

We find that the probability of extracting a single photon and reflecting it is limited by the directionality of the waveguide as we would intuitively expect. The extracted photon only travels in the correct direction with some probability less than unity. However as before, the probability of extracting a single photon from a pulsed coherent state is less than from a Fock state with the same number of photons. For the Fock state, this probability is independent of the number of photons above some threshold. This threshold is higher for waveguides with lower directionality.

Chapter 5

Conclusion

5.1 ARROW waveguides

We have looked at how the the propagation loss of a hollow core ARROW waveguide is affected by use of different cladding material pairs and the number of antiresonant layers. It is shown that using higher refracting index contrast materials and more antiresonant layers can decrease the propagation loss. We have also looked at how gratings can be implemented within the cladding structure of an ARROW to modulate the effective index of propagation. This has the advantage of leaving the hollow core unobstructed to allow the loading of atomic ensembles inside, which can be made to interact with tightly confined light. We demonstrated lossy mirrors with a reflectivity of up to 84% and unconventional cavities that can enhance the electric field intensity by up to 8×. We have also shown that even with the use of highly reflective dielectric metasurface mirrors, we can not achieve the high cooperativity regime or strong coupling regime for light-matter interaction due to the highly lossy nature of the hollow core ARROW waveguides.

5.2 Single photon extraction

Our calculations have shown how deterministic single photon extraction can be performed on an input pulse using a Λ scheme emitter coupled to a chiral waveguide. We have also shown that when continuously driving with a coherent state, we subtract exactly one photon from the input given that the atomic decay rate via emission into non-waveguide mode is much less than the waveguide-emitter coupling strength. We have also shown

that for Guassian pulsed coherent and Fock state inputs, the probability of single photon extraction is a function of the product of the temporal width and the waveguide emitter coupling strength, as well as the the number of photons in the input. For Fock state inputs, the probability of single photon extraction is independent of the number of photons above some threshold with the threshold being higher for larger interaction products. For non ideal chiral waveguides, we have shown that when continuously driving with coherent light, we extract more than one photon due to the imperfect directionality and the emitter decay. Also for coherent pulses and similar Fock state inputs, the probability of detecting the extracted single photon is limited by the directionality of the waveguide β. Some possible applications of our proposed system include photon number resolving detectors, attacks on quantum cryptography schemes, and quantum computation.

References

[1] Maksim Skorobogatiy. Microstructured and photonic bandgap fibers for applications in the resonant bio- and chemical sensors. *Journal of Sensors*, 2009, 2009.

[2] G. J. Pearce, G. S. Wiederhecker, C. G. Poulton, S. Burger, and P. St. J. Russell. Models for guidance in kagome-structured hollow-core photonic crystal fibres. *Opt. Express*, 15(20):12680–12685, Oct 2007.

[3] Evan J. Lunt. *Low-Loss Hollow Waveguide Platforms for Optical Sensing and Manipulation*. PhD thesis, Brigham Young University, 2010.

[4] Romeo Bernini, Stefania Campopiano, Luigi Zeni, and Pasqualina M Sarro. Arrow optical waveguides based sensors. *Sensors and Actuators B: Chemical*, 100(1-2):143 – 146, 2004. New materials and Technologies in Sensor Applications, Proceedings of the European Materials Research Society 2003 - Symposium N.

[5] Serge Rosenblum, Orel Bechler, Itay Shomroni, Yulia Lovsky, Gabriel Guendelman, and Barak Dayan. Extraction of a single photon from an optical pulse. *Nature Photonics*, 10(1):19–22, 2015.

[6] M. Bajcsy, S. Hofferberth, V. Balic, T. Peyronel, M. Hafezi, A. S. Zibrov, V. Vuletic, and M. D. Lukin. Efficient all-optical switching using slow light within a hollow fiber. *Phys. Rev. Lett.*, 102:203902, May 2009.

[7] Vivek Venkataraman, Kasturi Saha, and Alexander L Gaeta. Phase modulation at the few-photon level for weak-nonlinearity-based quantum computing. *Nature Photonics*, 7(2):138–141, 2013.

[8] M. R. Sprague, P. S. Michelberger, T. F. M. Champion, D. G. England, J. Nunn, X.-M. Jin, W. S. Kolthammer, A. Abdolvand, P. St. J. Russell, and I. a. Walmsley. Broadband single-photon-level memory in a hollow-core photonic crystal fibre. *Nature Photonics*, 8(4):287–291, 2014.

[9] Bin Wu, John F. Hulbert, Evan J. Lunt, Katie Hurd, Aaron R. Hawkins, and Holger Schmidt. Slow light on a chip via atomic quantum state control. *Nature Photonics*, 4(11):776–779, 2010.

[10] A Zavatta, V Parigi, M S Kim, and M Bellini. Subtracting photons from arbitrary light fields: experimental test of coherent state invariance by single-photon annihilation. *New Journal of Physics*, 10(12):123006, 2008.

[11] Valentina Parigi, Alessandro Zavatta, Myungshik Kim, and Marco Bellini. Probing quantum commutation rules by addition and subtraction of single photons to/from a light field. *Science*, 317(5846):1890–1893, 2007.

[12] Immo Söllner, Sahand Mahmoodian, Sofie Lindskov Hansen, Leonardo Midolo, Alisa Javadi, Gabija Kiršanskė, Tommaso Pregnolato, Haitham El-Ella, Eun Hye Lee, Jin Dong Song, Søren Stobbe, and Peter Lodahl. Deterministic photon-emitter coupling in chiral photonic circuits. *Nature Nanotechnology*, 10(9):775–778, 2015.

[13] Pochi Yeh, Amnon Yariv, and Emanuel Marom. Theory of bragg fiber∗. *J. Opt. Soc. Am.*, 68(9):1196–1201, Sep 1978.

[14] P. J. Roberts, F. Couny, H. Sabert, B. J. Mangan, D. P. Williams, L. Farr, M. W. Mason, A. Tomlinson, T. A. Birks, J. C. Knight, and P. St.J. Russell. Ultimate low loss of hollow-core photonic crystal fibres. *Opt. Express*, 13(1):236–244, Jan 2005.

[15] K. Nagayama, M. Kakui, M. Matsui, T. Saitoh, and Y. Chigusa. Ultra-low-loss (0.1484 db/km) pure silica core fibre and extension of transmission distance. *Electronics Letters*, 38:1168–1169(1), September 2002.

[16] F. Benabid. Inhibited-coupling guiding hollow core photonic crystal fibers. In *Lasers and Electro-Optics Europe (CLEO EUROPE/IQEC), 2013 Conference on and International Quantum Electronics Conference*, pages 1–1, May 2013.

[17] M. A. Duguay, Y. Kokubun, T. L. Koch, and Loren Pfeiffer. Antiresonant reflecting optical waveguides in $SiO_2 - Si$ multilayer structures. *Applied Physics Letters*, 49(1):13–15, 1986.

[18] Thomas Delonge and Henning Fouckhardt. 7th international symposium on high performance capillary electrophoresis integrated optical detection cell based on bragg reflecting waveguides. *Journal of Chromatography A*, 716(1):135 – 139, 1995.

[19] L. J. Mawst, D. Botez, C. Zmudzinski, and C. Tu. Design optimization of arrow-type diode lasers. *IEEE Photonics Technology Letters*, 4(11):1204–1206, Nov 1992.

[20] Holger Schmidt and Aaron R. Hawkins. Optofluidic waveguides: I. concepts and implementations. *Microfluidics and Nanofluidics*, 4(1):3–16, 2008.

[21] Brian J. Phillips. *Tailoring the Spectral Transmission of Optofluidic Waveguides*. PhD thesis, Brigham Young University, 2011.

[22] D. Yin, H. Schmidt, J.P. Barber, and A.R. Hawkins. Integrated arrow waveguides with hollow cores. *Opt. Express*, 12(12):2710–2715, Jun 2004.

[23] Dongliang Yin, John P. Barber, Aaron R. Hawkins, and Holger Schmidt. Waveguide loss optimization in hollow-core arrow waveguides. *Opt. Express*, 13(23):9331–9336, Nov 2005.

[24] Y. Zhao, M. Jenkins, P. Measor, K. Leake, S. Liu, H. Schmidt, and A. R. Hawkins. Hollow waveguides with low intrinsic photoluminescence fabricated with ta2o5 and sio2 films. *Applied Physics Letters*, 98(9), 2011.

[25] E. J. Lunt, B. Wu, J. M. Keeley, P. Measor, H. Schmidt, and A. R. Hawkins. Hollow arrow waveguides on self-aligned pedestals for improved geometry and transmission. *IEEE Photonics Technology Letters*, 22(15):1147–1149, Aug 2010.

[26] J. P. Barber, D. B. Conkey, J. R. Lee, N. B. Hubbard, L. L. Howell, Dongliang Yin, H. Schmidt, and A. R. Hawkins. Fabrication of hollow waveguides with sacrificial aluminum cores. *IEEE Photonics Technology Letters*, 17(2):363–365, Feb 2005.

[27] Kirt R. Williams, Kishan Gupta, and Matthew Wasilik. Etch rates for micromachining processing - Part II. *Journal of Microelectromechanical Systems*, 12(6):761–778, 2003.

[28] Andreas Othonos. Fiber bragg gratings. *Review of Scientific Instruments*, 68(12):4309–4341, 1997.

[29] E. Hecht. *Optics*. Addison-Wesley, 4th edition, 1998.

[30] H.V. Baghdasaryan, T.M. Knyazyan, T.H. Baghdasaryan, B. Witzigmann, and F. Roemer. Absorption loss influence on optical characteristics of multilayer distributed bragg reflector: wavelength-scale analysis by the method of single expression. *Opto-Electronics Review*, 18(4):438–445, 2010.

[31] Virginie Lousse, Wonjoo Suh, Onur Kilic, Sora Kim, Olav Solgaard, and Shanhui Fan. Angular and polarization properties of a photonic crystal slab mirror. *Opt. Express*, 12(8):1575–1582, Apr 2004.

[32] H J Kimble. Strong interactions of single atoms and photons in cavity qed. *Physica Scripta*, 1998(T76):127, 1998.

[33] K Hennessy, A Badolato, M Winger, D Gerace, M. Atature, S Gulde, S. Falt, E L Hu, and A. Imamoglu. Quantum nature of a strongly-coupled single quantum dot-cavity system. *Nature*, 445(February):896, 2007.

[34] Alexei Ourjoumtsev, Aurélien Dantan, Rosa Tualle-Brouri, and Philippe Grangier. Increasing entanglement between gaussian states by coherent photon subtraction. *Phys. Rev. Lett.*, 98:030502, Jan 2007.

[35] T. Opatrný, G. Kurizki, and D.-G. Welsch. Improvement on teleportation of continuous variables by photon subtraction via conditional measurement. *Phys. Rev. A*, 61:032302, Feb 2000.

[36] A Gilchrist, Kae Nemoto, W J Munro, T C Ralph, S Glancy, Samuel L Braunstein, and G J Milburn. Schrdinger cats and their power for quantum information processing. *Journal of Optics B: Quantum and Semiclassical Optics*, 6(8):S828, 2004.

[37] Jan Petersen, Jürgen Volz, and Arno Rauschenbeutel. Chiral nanophotonic waveguide interface based on spin-orbit interaction of light. *Science*, 346(6205):67–71, 2014.

[38] C. W. Gardiner and M. J. Collett. Input and output in damped quantum systems: Quantum stochastic differential equations and the master equation. *Phys. Rev. A*, 31:3761–3774, Jun 1985.

[39] Shanhui Fan, Şükrü Ekin Kocabaş, and Jung-Tsung Shen. Input-output formalism for few-photon transport in one-dimensional nanophotonic waveguides coupled to a qubit. *Phys. Rev. A*, 82:063821, Dec 2010.

[40] Şükrü Ekin Kocabaş, Eden Rephaeli, and Shanhui Fan. Resonance fluorescence in a waveguide geometry. *Phys. Rev. A*, 85:023817, Feb 2012.

[41] Rodney Loudon. *The Quantum Theory of Light*. Oxford University Press, 2000.

APPENDICES

Appendix A

Waveguide and FEM simulation parameters

Table A.1: Finite element modelling simulation parameters

Wavelength	852 nm
Simulation region width[1]	200 μm
Perfectly Matched Layer (PML) width[2]	20 μm
Number of divisions per element[3]	17

Table A.2: Self aligned pedestal ARROW parameters

Pedestal height[4]	6 μm
Si_3N_4/TiO_2 conformality ratio[5]	1.25
SiO_2 conformality ratio[5]	1.58
SiO_2 conformality ratio[5] (top thick layer)	1.63

1. Using larger values of the simulation region width yields more accurate results from the mode solver, but at the expense of more computational time.

2. PML refers to boundaries that absorb any outgoing radiation. The width determines how much radiation can be absorbed. A thicker PML yields more accurate results from the mode solver.

3. The waveguide cross section is modelled by combining multiple elements. This parameter determines how precisely each element is discretized when using the mode solver.

4. The height of the pedestal on silicon substrate as shown in Figure 2.5a.

5. Ratio of the top film thickness above the core to the side film thickness (Figure 2.5a).

Table A.3: Layer thicknesses of optimized 3 period hollow core ARROWs using $Si_3N_4(1.74)/SiO_2$ cladding layers for various core sizes

	$5.8\mu m \times 8\mu m$	$5.8\mu m \times 12\mu m$	$10.6\mu m \times 22\mu m$	$13\mu m \times 27\mu m$
Propagation Loss (cm^{-1})	6.536	0.87	0.118	0.052
n_{low} (top)	5.163 μm	5.917 μm	5.702 μm	2.475 μm
n_{high}	250 nm	65 nm	250 nm	235 nm
n_{low}	128 nm	291 nm	166 nm	145 nm
n_{high}	65 nm	172 nm	84 nm	241 nm
n_{low}	339 nm	175 nm	329 nm	197 nm
n_{high}	325 nm	81 nm	370 nm	377 nm
n_{core}	5.8 μm	5.8 μm	5.8 μm	5.8 μm
n_{high}	280 nm	213 nm	219 nm	100 nm
n_{low}	157 nm	173 nm	82 nm	364 nm
n_{high}	103 nm	90 nm	349 nm	259 nm
n_{low}	271 nm	174 nm	362 nm	408 nm
n_{high}	67 nm	180 nm	219 nm	390 nm
n_{low} (bottom)	338 nm	268 nm	120 nm	421 nm

Table A.4: Layer thicknesses of optimized 2 period hollow core ($5.8\mu m \times 12\mu m$) ARROWs with high index layer beneath the core

	$n_{high} = 1.74$ $n_{low} = 1.44$	$n_{high} = 2$ $n_{low} = 1.44$	$n_{high} = 2.4$ $n_{low} = 1.44$
Propagation Loss (cm^{-1})	1.68	1.46	1.38
n_{low} (top)	4.8 μm	2.534 μm	4.689 μm
n_{high}	378 nm	159 nm	112 nm
n_{low}	265 nm	157 nm	292 nm
n_{high}	109 nm	359 nm	263 nm
n_{core}	5.8 μm	5.8 μm	5.8 μm
n_{high}	260 nm	262 nm	146 nm
n_{low}	229 nm	183 nm	364 nm
n_{high}	271 nm	249 nm	76 nm
n_{low} (bottom)	190 nm	310 nm	352 nm

Table A.5: Layer thicknesses of optimized 3 period hollow core ($5.8\mu m \times 12\mu m$) ARROWs with high index layer beneath the core

	$n_{high} = 1.74$ $n_{low} = 1.44$	$n_{high} = 2$ $n_{low} = 1.44$	$n_{high} = 2.4$ $n_{low} = 1.44$
Propagation Loss (cm^{-1})	0.87	0.86	0.77
n_{low} (top)	5.917 μm	3.604 μm	2.479 μm
n_{high}	65 nm	194 nm	148 nm
n_{low}	291 nm	429 nm	258 nm
n_{high}	172 nm	120 nm	112 nm
n_{low}	175 nm	327 nm	215 nm
n_{high}	81 nm	306 nm	276 nm
n_{core}	5.8 μm	5.8 μm	5.8 μm
n_{high}	213 nm	92 nm	387 nm
n_{low}	173 nm	209 nm	107 nm
n_{high}	90 nm	166 nm	243 nm
n_{low}	174 nm	486 nm	187 nm
n_{high}	180 nm	422 nm	366 nm
n_{low} (bottom)	268 nm	278 nm	323 nm

Table A.6: Layer thicknesses of optimized 4 period hollow core ($5.8\mu m \times 12\mu m$) ARROWs with high index layer beneath the core

	$n_{high} = 1.74$ $n_{low} = 1.44$	$n_{high} = 2$ $n_{low} = 1.44$	$n_{high} = 2.4$ $n_{low} = 1.44$
Propagation Loss (cm^{-1})	0.56	0.38	0.65
n_{low} (top)	3.59 μm	4.538 μm	4.669 μm
n_{high}	87 nm	220 nm	64 nm
n_{low}	217 nm	175 nm	463 nm
n_{high}	182 nm	362 nm	362 nm
n_{low}	130 nm	345 nm	303 nm
n_{high}	349 nm	229 nm	392 nm
n_{low}	78 nm	299 nm	99 nm
n_{high}	69 nm	354 nm	55 nm
n_{core}	5.8 μm	5.8 μm	5.8 μm
n_{high}	155 nm	243 nm	377 nm
n_{low}	304 nm	78 nm	142 nm
n_{high}	74 nm	174 nm	100 nm
n_{low}	260 nm	74 nm	249 nm
n_{high}	335 nm	291 nm	293 nm
n_{low}	219 nm	96 nm	203 nm
n_{high}	85 nm	364 nm	367 nm
n_{low} (bottom)	127 nm	133 nm	276 nm

Table A.7: Layer thicknesses of optimized 2 period hollow core ($5.8\mu m \times 12\mu m$) ARROWs with low index layer beneath the core

	$n_{high} = 1.74$ $n_{low} = 1.44$	$n_{high} = 2$ $n_{low} = 1.44$	$n_{high} = 2.4$ $n_{low} = 1.44$
Propagation Loss (cm^{-1})	1.74	1.38	1.24
n_{low} (top)	4.176 μm	3.105 μm	3.045 μm
n_{high}	219 nm	80 nm	86 nm
n_{low}	427 nm	217 nm	409 nm
n_{high}	154 nm	384 nm	219 nm
n_{core}	5.8 μm	5.8 μm	5.8 μm
n_{low}	211 nm	265 nm	79 nm
n_{high}	231 nm	266 nm	177 nm
n_{low}	290 nm	263 nm	380 nm
n_{high} (bottom)	101 nm	171 nm	313 nm

Table A.8: Layer thicknesses of optimized 3 period hollow core ($5.8\mu m \times 12\mu m$) ARROWs with low index layer beneath the core

	$n_{high} = 1.74$ $n_{low} = 1.44$	$n_{high} = 2$ $n_{low} = 1.44$	$n_{high} = 2.4$ $n_{low} = 1.44$
Propagation Loss (cm^{-1})	1.11	0.9	0.74
n_{low} (top)	2.98 μm	5.417 μm	4.742 μm
n_{high}	239 nm	364 nm	88 nm
n_{low}	231 nm	142 nm	411 nm
n_{high}	62 nm	346 nm	328 nm
n_{low}	239 nm	220 nm	206 nm
n_{high}	210 nm	331 nm	323 nm
n_{core}	5.8 μm	5.8 μm	5.8 μm
n_{low}	473 nm	341 nm	473 nm
n_{high}	125 nm	189 nm	343 nm
n_{low}	71 nm	249 nm	139 nm
n_{high}	73 nm	64 nm	80 nm
n_{low}	392 nm	444 nm	313 nm
n_{high} (bottom)	355 nm	126 nm	248 nm

Table A.9: Layer thicknesses of optimized 4 period hollow core ($5.8\mu m \times 12\mu m$) ARROWs with low index layer beneath the core

	$n_{high} = 1.74$ $n_{low} = 1.44$	$n_{high} = 2$ $n_{low} = 1.44$	$n_{high} = 2.4$ $n_{low} = 1.44$
Propagation Loss (cm^{-1})	0.93	0.61	0.24
n_{low} (top)	2.931 μm	3.096 μm	2.46 μm
n_{high}	264 nm	409 nm	108 nm
n_{low}	283 nm	335 nm	217 nm
n_{high}	81 nm	245 nm	396 nm
n_{low}	166 nm	231 nm	417 nm
n_{high}	388 nm	469 nm	112 nm
n_{low}	305 nm	125 nm	183 nm
n_{high}	381 nm	122 nm	293 nm
n_{core}	5.8 μm	5.8 μm	5.8 μm
n_{low}	220 nm	374 nm	396 nm
n_{high}	121 nm	72 nm	58 nm
n_{low}	152 nm	257 nm	304 nm
n_{high}	323 nm	377 nm	233 nm
n_{low}	83 nm	410 nm	220 nm
n_{high}	272 nm	405 nm	194 nm
n_{low}	198 nm	174 nm	183 nm
n_{high} (bottom)	325 nm	486 nm	211 nm

Appendix B

Python code for single photon extraction calculations

B.1 Continuously driven coherent input

```
import numpy as np
import scipy.linalg as lin
import matplotlib.pyplot as plt
import numpy.matlib


V1 = np.sqrt(10)
V2 = np.sqrt(10)
beta = 1
VR1 = np.sqrt(beta)*V1
VL2 = np.sqrt(beta)*V2
VL1 = np.sqrt(1-beta)*V1
VR2 = np.sqrt(1-beta)*V2
alpha = np.sqrt(2*np.pi*10)
gamma1 = 0
gamma2 = gamma1

x0 = np.matrix([[0],[0],[0],[1],[0]])
```

```
M = np.matrix([[-(np.pi*(VR1**2+VL1**2+VR2**2+VL2**2)+gamma1+
    gamma2),0,1j*VR1*alpha,-1j*VR1*alpha,0],
                   [0,-(np.pi*(VR1**2+VL1**2+VR2**2+VL2**2)+gamma1+
                       gamma2),-1j*VR1*alpha,1j*VR1*alpha,0],
                   [1j*VR1*alpha,-1j*VR1*alpha,-2*(np.pi*(VR1**2+VL1
                       **2+VR2**2+VL2**2)+gamma1+gamma2),0,0],
                   [-1j*VR1*alpha,1j*VR1*alpha,2*(np.pi*(VR1**2+VL1
                       **2)+gamma1),0,0],
                   [0,0,2*(np.pi*(VR2**2+VL2**2)+gamma2),0,0]])

t = np.linspace(0,1,1001)
g1 = np.zeros(len(t))
g2 = np.zeros(len(t))
lout1 = np.zeros(len(t))
lout2 = np.zeros(len(t))
rout1 = np.zeros(len(t))
rout2 = np.zeros(len(t))

g1[0] = 1
rout1[0] = alpha**2/(2*np.pi)

for i in range(1,len(t)):
    x = lin.expm(M*t[i])*x0
    g1[i] = abs(x.item(3))
    g2[i] = abs(x.item(4))
    lout1[i] = 2*np.pi*(VL1**2)*abs(x.item(2))
    lout2[i] = 2*np.pi*(VL2**2)*abs(x.item(2))
    rout1[i] = abs(alpha**2/(2*np.pi)+1j*VR1*(alpha*x.item(1)-
        alpha*x.item(0))+2*np.pi*VR1**2*x.item(2))
    rout2[i] = 2*np.pi*(VR2**2)*abs(x.item(2))

plt.plot(t,lout2/rout1[0],linewidth=1.5,label=r'$\langle␣l^{\dag}
    _{2,out}␣l_{2,out}␣\rangle$')
plt.plot(t,rout1/rout1[0],linewidth=1.5,label=r'$\langle␣r^{\dag}
    _{1,out}␣r_{1,out}␣\rangle$')
plt.plot(t,g2*beta,linewidth=1.5,label=r'$\int_{0}^{t}␣\langle␣l
    ^{\dag}_{2,out}␣l_{2,out}␣\rangle$')
plt.plot(t,g2*VL1**2/(VR2**2+VL2**2),linewidth=1.5,label=r'$\int_
```

```
    {0}^{t}␣\langle␣l^{\dag}_{1,out}␣l_{1,out}␣\rangle$')
plt.plot(t,g2*(1-beta),linewidth=1.5,label=r'$\int_{0}^{t}␣\
    langle␣r^{\dag}_{2,out}␣r_{2,out}␣\rangle$')
plt.plot(t,g1,linewidth=1.5,label=r'$\langle␣\sigma_{11}␣\rangle$
    ')
plt.xlabel('time')
plt.title(r'$V^{2}␣=␣%g,␣\beta␣=␣%g,␣\gamma␣=␣%g,␣|\alpha|^{2}␣=␣
    %g$' %(V1**2,beta,gamma1,alpha**2/(2*np.pi)),fontsize=20)
plt.legend(loc=0)
plt.savefig('3LS_expectation_values_V_%g_beta_%g_gamma_%g_alpha_%
    g.pdf' %(V1**2,beta,gamma1,alpha**2/(2*np.pi)))
```

B.2 Coherent input pulse

```
import numpy as np
import scipy.linalg as lin
import matplotlib.pyplot as plt
import time as timer


def f( t, tau ):
    return np.sqrt(2)*np.exp(-2*(t/tau)**2)/np.power(np.pi*tau
        **2,1/4)

V1 = np.sqrt(10)
V2 = np.sqrt(10)
beta = 1
VR1 = np.sqrt(beta)*V1
VL2 = np.sqrt(beta)*V2
VL1 = np.sqrt(1-beta)*V1
VR2 = np.sqrt(1-beta)*V2
alpha = np.sqrt(5)
gamma1 = 0
gamma2 = gamma1
tau = 1

x0 = np.matrix([[0],[0],[0],[1],[0]])
```

```
t = np.linspace(-5*tau,5*tau,50001)
g1 = np.zeros(len(t))
g2 = np.zeros(len(t))
lout1 = np.zeros(len(t))
lout2 = np.zeros(len(t))
rout1 = np.zeros(len(t))
rout2 = np.zeros(len(t))
rout1int = np.zeros(len(t),dtype=np.complex)

g1[0] = 1
rout1[0] = abs(alpha*f(t[0],tau))**2
x = x0

start = timer.time()

for i in range(1,len(t)):
    M = np.matrix([[-(np.pi*(VR1**2+VL1**2+VR2**2+VL2**2)+gamma1+
        gamma2),0,1j*np.sqrt(2*np.pi)*VR1*alpha*f(t[i],tau),-1j*np
        .sqrt(2*np.pi)*VR1*alpha*f(t[i],tau),0],
                   [0,-(np.pi*(VR1**2+VL1**2+VR2**2+VL2**2)+
                       gamma1+gamma2),-1j*np.sqrt(2*np.pi)*VR1*
                       alpha*f(t[i],tau),1j*np.sqrt(2*np.pi)*VR1*
                       alpha*f(t[i],tau),0],
                   [1j*np.sqrt(2*np.pi)*VR1*alpha*f(t[i],tau),-1j
                       *np.sqrt(2*np.pi)*VR1*alpha*f(t[i],tau)
                       ,-2*(np.pi*(VR1**2+VL1**2+VR2**2+VL2**2)+
                       gamma1+gamma2),0,0],
                   [-1j*np.sqrt(2*np.pi)*VR1*alpha*f(t[i],tau),1j
                       *np.sqrt(2*np.pi)*VR1*alpha*f(t[i],tau),2*(
                       np.pi*(VR1**2+VL1**2)+gamma1),0,0],
                   [0,0,2*(np.pi*(VR2**2+VL2**2)+gamma2),0,0]])

    x = x + (t[i]-t[i-1])*M*x
    g1[i] = abs(x.item(3))
    g2[i] = abs(x.item(4))
    lout1[i] = 2*np.pi*(VL1**2)*abs(x.item(2))
    lout2[i] = 2*np.pi*(VL2**2)*abs(x.item(2))
```

```
    rout1[i] = abs(abs(alpha*f(t[i],tau))**2+1j*VR1*(alpha*f(t[i
        ],tau)*x.item(1)-alpha*f(t[i],tau)*x.item(0))+2*np.pi*VR1
        **2*x.item(2))
    rout1int[i] = rout1int[i-1] + (1j*VR1*(alpha*f(t[i],tau)*x.
        item(1)-alpha*f(t[i],tau)*x.item(0))+2*np.pi*VR1**2*x.item
        (2))*(t[i]-t[i-1])
    rout2[i] = 2*np.pi*(VR2**2)*abs(x.item(2))

print((timer.time()-start)/60)

plt.plot(t,lout2,linewidth=1.5,label=r'$\langle l^{\dag}_{2,out}
    l_{2,out}\rangle$')
plt.plot(t,rout1,linewidth=1.5,label=r'$\langle r^{\dag}_{1,out}
    r_{1,out}\rangle$')
plt.plot(t,g2*beta,linewidth=1.5,label=r'$\int_{0}^{t}\langle l
    ^{\dag}_{2,out}l_{2,out}\rangle$')
plt.plot(t,g2*(1-beta),linewidth=1.5,label=r'$\int_{0}^{t}\
    langle r^{\dag}_{2,out}r_{2,out}\rangle$')
plt.plot(t,g1,linewidth=1.5,label=r'$\langle \sigma_{11}\rangle$
    ')
plt.xlabel('time')
plt.xlim(t[0],t[-1])
plt.title(r'$V^{2} = %g, \beta = %g, \gamma = %g, \langle n \
    rangle = %g, \tau = %g$' %(VR1**2,beta,gamma1,alpha**2,tau),
    fontsize=20)
plt.legend(loc=0)
plt.savefig('3LS_expectation_values_pulsed_V_%g_beta_%g_gamma_%
    g_n_%g_tau_%g.pdf' %(VR1**2,beta,gamma1,alpha**2,tau))
```

B.3 Fock state input

```
import numpy as np
import scipy.linalg as lin
import matplotlib.pyplot as plt
import time as timer
```

```
def f( t, tau ):
    return np.sqrt(2)*np.exp(-2*(t/tau)**2)/np.power(np.pi*tau
        **2,1/4)

V1 = np.sqrt(10)
V2 = np.sqrt(10)
beta = 1
VR1 = np.sqrt(beta)*V1
VL2 = np.sqrt(beta)*V2
VL1 = np.sqrt(1-beta)*V1
VR2 = np.sqrt(1-beta)*V2
N = 10
gamma1 = 0
gamma2 = gamma1
tau = 1

t = np.linspace(-5*tau,5*tau,50001)

g1 = np.zeros((N+1,len(t)))
lout2 = np.zeros((N+1,len(t)))
rout1 = np.zeros((N+1,len(t)),dtype=np.complex)
rout2 = np.zeros((N+1,len(t)))
lout2int = np.zeros((N+1,len(t)))
rout1int = np.zeros((N+1,len(t)),dtype=np.complex)
rout2int = np.zeros((N+1,len(t)))

M = np.matlib.zeros((4*(N+1)**2,4*(N+1)**2),dtype=np.complex)
x = np.matlib.zeros((4*(N+1)**2,1))

start = timer.time()

for i in range(N+1):
    x[4*((N+1)*i+i)+3] = 1
    g1[i][0] = 1
    rout1[i][0] = i*f(t[0],tau)**2
    for j in range(N+1):
        M[4*((N+1)*i+j),4*((N+1)*i+j)] = -(np.pi*(VR1**2+VL1**2+
            VR2**2+VL2**2)+gamma1+gamma2)
```

```
        M[4*((N+1)*i+j)+1,4*((N+1)*i+j)+1] = -(np.pi*(VR1**2+VL1
            **2+VR2**2+VL2**2)+gamma1+gamma2)
        M[4*((N+1)*i+j)+2,4*((N+1)*i+j)+2] = -2*(np.pi*(VR1**2+
            VL1**2+VR2**2+VL2**2)+gamma1+gamma2)
        M[4*((N+1)*i+j)+3,4*((N+1)*i+j)+2] = 2*(np.pi*(VR1**2+VL1
            **2)+gamma1)


for i in range(1,len(t)):
    for j in range(N+1):
        for k in range(N+1):
            if k >= 1:
                M[4*((N+1)*j+k),4*((N+1)*j+k-1)+2] = 1j*np.sqrt
                    (2*np.pi)*VR1*np.sqrt(k)*f(t[i],tau)
                M[4*((N+1)*j+k),4*((N+1)*j+k-1)+3] = -1j*np.sqrt
                    (2*np.pi)*VR1*np.sqrt(k)*f(t[i],tau)

                M[4*((N+1)*j+k)+2,4*((N+1)*j+k-1)+1] = -1j*np.
                    sqrt(2*np.pi)*VR1*np.sqrt(k)*f(t[i],tau)
                M[4*((N+1)*j+k)+3,4*((N+1)*j+k-1)+1] = 1j*np.sqrt
                    (2*np.pi)*VR1*np.sqrt(k)*f(t[i],tau)

            if j >= 1:
                M[4*((N+1)*j+k)+1,4*((N+1)*(j-1)+k)+2] = -1j*np.
                    sqrt(2*np.pi)*VR1*np.sqrt(j)*f(t[i],tau)
                M[4*((N+1)*j+k)+1,4*((N+1)*(j-1)+k)+3] = 1j*np.
                    sqrt(2*np.pi)*VR1*np.sqrt(j)*f(t[i],tau)

                M[4*((N+1)*j+k)+2,4*((N+1)*(j-1)+k)] = 1j*np.sqrt
                    (2*np.pi)*VR1*np.sqrt(j)*f(t[i],tau)
                M[4*((N+1)*j+k)+3,4*((N+1)*(j-1)+k)] = -1j*np.
                    sqrt(2*np.pi)*VR1*np.sqrt(j)*f(t[i],tau)

    x = x + (t[i]-t[i-1])*M*x
    for j in range(N+1):
        g1[j][i] = abs(x.item(4*((N+1)*j+j)+3))
        rout1[j][i] = j*f(t[i],tau)**2 + 1j*np.sqrt(2*np.pi)*VR1*
            np.sqrt(j)*f(t[i],tau)*(x.item(4*((N+1)*j+j)+1)-x.item
```

```
            (4*((N+1)*j+j)))+2*np.pi*VR1**2*x.item(4*((N+1)*j+j)
            +2)
        lout2[j][i] = 2*np.pi*VL2**2*abs(x.item(4*((N+1)*j+j)+2))
        rout2[j][i] = 2*np.pi*VR2**2*abs(x.item(4*((N+1)*j+j)+2))
        rout1int[j][i] = rout1int[j][i-1] + rout1[j][i]*(t[i]-t[i
            -1])
        lout2int[j][i] = lout2int[j][i-1] + lout2[j][i]*(t[i]-t[i
            -1])
        rout2int[j][i] = rout2int[j][i-1] + rout2[j][i]*(t[i]-t[i
            -1])

print((timer.time()-start)/60)

plt.plot(t,lout2[N],linewidth=1.5,label=r'$\langle␣l^{\dag}_{out
    ,2}␣l_{out,2}␣\rangle$')
plt.plot(t,lout2int[N],linewidth=1.5,label=r'$\int_{-\infty}^{t}␣
    \langle␣l^{\dag}_{out,2}␣l_{out,2}␣\rangle␣dt^{\prime}$')
plt.plot(t,g1[N],linewidth=1.5,label=r'$\langle␣\sigma_{11}␣\
    rangle$')
plt.xlabel('time',fontsize=18)
plt.xlim(t[0],t[-1])
plt.title(r'$V^{2}␣=␣%g,␣\beta␣=␣%g,␣\gamma␣=␣%g,␣N␣=␣%g,␣\tau␣=␣
    %g$' %(VR1**2,beta,gamma1,N,tau),fontsize=20)
plt.legend(loc=0,fontsize=18)
plt.savefig('3LS_Fock_expectation_values_V_%g_beta_%g_gamma_%g_N_
    %g_tau_%g.pdf' %(VR1**2,beta,gamma1,N,tau))

plt.clf()

plt.plot(range(1,N+1),1-lout2int[1:,-1],'o',linewidth=1.5,label=r
    '$P_{L2}$')
plt.plot(range(1,N+1),1-rout2int[1:,-1],'o',linewidth=1.5,label=r
    '$P_{R2}$')
plt.plot(range(1,N+1),1-(lout2int[1:,-1]+rout2int[1:,-1]),'o',
    linewidth=1.5,label=r'$P_{L2}+P_{R2}$')
plt.xlabel(r'$N$',fontsize=18)
plt.ylabel(r'$1-P$',fontsize=18)
plt.yscale('log')
```

```
plt.xticks(range(N+2))
plt.legend(loc=0,fontsize=18)
plt.title(r'$V^{2} = %g, \beta = %g, \gamma = %g, \tau = %g$' %(
    VR1**2,beta,gamma1,tau),fontsize=18)
plt.savefig('3LS_Fock_prob_V_%g_beta_%g_gamma_%g_tau_%g.pdf' %(
    VR1**2,beta,gamma1,tau))
```